

RESEARCH

Open Access



TDP43 augments astrocyte inflammatory activity through mtDNA-cGAS-STING axis in NMOSD

Zhuhe Liu^{1†}, Yunmeng Bai^{2†}, Bingtian Xu^{1*†}, Haixia Wen¹, Kechun Chen³, Jingfang Lin¹, Yuanyuan Wang¹, Jiangping Xu³, Haitao Wang³, Fudong Shi^{4,5*}, Jigang Wang^{2*} and Honghao Wang^{1*}

Abstract

Abnormality in transactivating response region DNA binding protein 43 (TDP43) is well-recognized as the pathological hallmark of neurodegenerative diseases. However, the role of TDP43 in neuromyelitis optica spectrum disorder (NMOSD) remains unknown. Here, our observations demonstrate an upregulation of TDP43 in both in vitro and in vivo models of NMOSD, as well as in biological samples from NMOSD patients. Single-nucleus RNA sequencing revealed that NMOSD induced A1-like reactive astrocytes and astrocyte mitochondrial dysfunction in mice. We further found that NMOSD provoked the translocation of TDP43 to mitochondria and the release of mitochondrial DNA (mtDNA) into the cytoplasm. NMOSD caused activation of mtDNA/cyclic GMP-AMP synthase (cGAS) / stimulator of interferon genes (STING) pathway and A1-type inflammatory activation in astrocytes. Crucially, the knockdown of TDP43 markedly ameliorated NMOSD-induced mitochondrial dysfunction and the activation of the cGAS/STING pathway in astrocytes. Conversely, overexpression of TDP43 exacerbated these pathological changes. Specific silencing astrocytic TDP43 ameliorated NMOSD-induced injury in mice, and conversely, TDP43 overexpression intensified the injury. Meanwhile, both cGAS and STING inhibitors attenuated NMOSD-induced injury in mice. In summary, our data suggest that TDP43 exacerbates inflammatory activation of astrocytes in NMOSD through upregulating the mtDNA/cGAS/STING signaling pathway. Therefore, targeting TDP43 represents a compelling therapeutic strategy for NMOSD.

Keywords TDP43, NMOSD, cGAS/STING, Mitochondrial dysfunction, Inflammatory activation

[†]Zhuhe Liu, Yunmeng Bai and Bingtian Xu contributed equally to this work.

*Correspondence:

Bingtian Xu
eyxubingtian@scut.edu.cn
Fudong Shi
fshi@tmu.edu.cn
Jigang Wang
jgwang@icmm.ac.cn
Honghao Wang
wang_whh@163.com

¹Department of Neurology, Center for Medical Research on Innovation and Translation, Institute of Clinical Medicine, Guangzhou First People's

Hospital, School of Medicine, South China University of Technology, Guangzhou, China

²Department of Nephrology, Shenzhen Key Laboratory of Kidney Diseases, The First Affiliated Hospital, School of Medicine, Shenzhen People's Hospital, Southern University of Science and Technology, Shenzhen, China

³Guangdong Provincial Key Laboratory of New Drug Screening, School of Pharmaceutical Sciences, Southern Medical University, Guangzhou, China

⁴Department of Neurology, China National Clinical Research Center for Neurological Diseases, Beijing Tiantan Hospital, Capital Medical University, Beijing, China

⁵Department of Neurology, Tianjin Neurological Institute, Tianjin Medical University General Hospital, Tianjin, China



Introduction

Neuromyelitis optica spectrum disorder (NMOSD) represents an inflammatory demyelinating disease that is distinguished by the detection of serum aquaporin 4 (AQP4)-IgG antibodies [1]. Although treatments like corticosteroids, plasma exchange, immunoglobulins, and immunosuppressants are employed, a definitive cure remains elusive [2]. Consequently, delving into the underlying mechanisms of NMOSD to unearth potential targets for intervention and therapeutic strategies is imperative.

Astrocytes are recognized as the key compromised cells during the pathological cascade of NMOSD. Common consensus holds that AQP4-IgG triggers astrocyte damage and activation, leading to demyelination, neuronal damage, and subsequent neurological deficits [3, 4]. However, the intricate mechanisms that govern astrocyte activation remain not completely understood.

Recent researches indicate that mitochondrial dysfunction and metabolic alterations could be implicated in the progression of NMOSD [5, 6]. Clinical investigations have illuminated the significant role of mitochondrial dysfunction in disease progression, degrees of disability, and cognitive deterioration among patients with NMOSD [7]. Detailed analyses focused on glial cells and axons within the anterior visual pathway have uncovered enhanced mitochondrial degeneration within the ocular lesion tissues of NMOSD patients [8]. Recent study has showed that AQP4-IgG increased DNA damage and caused astrocytic damage, which suggest DNA damage in astrocyte in NMO [9]. Furthermore, research posits that following exposure to AQP4-IgG, the release of mitochondrial DNA (mtDNA) by astrocytes is a pivotal factor in the creation of an inflammatory cascade that facilitates monocyte recruitment and activation [10]. Mitochondria are pivotal to the metabolic functions of astrocytes [11]. Perturbations affecting mitochondrial respiratory chain function, dynamic equilibrium, and autophagic processes within astrocytes contribute to neurological conditions like epilepsy, cerebral ischemia, Alzheimer's disease, Parkinson's disease, and NMOSD [6, 12–15]. Identifying strategies to protect mitochondria from damage is essential for reducing inflammation and preserving astrocyte function in conditions like NMOSD.

The transactivating response region DNA binding protein 43 (TDP43) is a crucial DNA and RNA binding protein that orchestrates vital cellular undertakings including RNA splicing, transport, and stabilization [16]. TDP43 is ubiquitously expressed in both neurons and glial cells. Although previous researches have centered on neuronal TDP43, the occurrence of TDP43 pathology in glial cells is equally noteworthy [17]. Astrocytes differentiated from pluripotent stem cells of amyotrophic lateral sclerosis (ALS) patients, exhibit cytoplasmic TDP43

aggregates [18]. The aberrant cytoplasmic accrual of TDP43 in astrocytes has been associated with compromised memory [19], and the presence of the ALS-linked TDP43 M337V mutation, or a reduction in TDP43 levels, can lead to motor deficits [20, 21]. TDP43 pathologies can also instigate mitochondrial dysfunction, impair mitophagy, and prompt a cascade of other complications typical of neurodegenerative conditions [22, 23]. All in all, abnormalities in TDP43 and subsequent mitochondrial dysfunction are significant contributors to neurological and psychiatric disorders. Nevertheless, the role of TDP43 in NMOSD is still unknown, demanding further exploration.

The cyclic GMP-AMP synthase (cGAS) operates as a sensor of double-stranded DNA, capable of identifying aberrant DNA sequences and facilitating the transformation of ATP and GTP into the secondary messenger 2'3' cyclic GMP-AMP (cGAMP) [24]. Following synthesis, cGAMP interacts with stimulator of interferon genes (STING) located on the endoplasmic reticulum (ER) membrane, initiating its migration towards the Golgi apparatus and the subsequent phosphorylation of TANK-binding kinase 1, then activates interferon regulatory factor 3, and finally stimulates the transcription of interferon-stimulating genes [25]. The cGAS/STING signaling axis is pivotal in mediating responses across a spectrum of pathological contexts, including immune responses [26]. Studies have suggested that mitochondrial stress and subsequent DNA leakage as potential activators of this pathway, leading to neuroinflammatory responses [27]. Post-mitochondrial distress, the released mtDNA constitutes a substrate for cGAS recognition and binding [28], proposing cGAS/STING signaling as a consequential pathway following the aberrant aggregation of TDP43 and ensuing mitochondrial impairment. In CNS, the emphasis on cGAS/STING research has predominantly been associated with microglial activation and neuronal damage [27, 29]. However, the precise involvement of this pathway in the inflammatory activation of astrocytes in NMOSD remains unclear and warrants further investigation.

This study aims to investigate the link between the abnormal accumulation of TDP43 and the inflammatory activation of astrocytes in NMOSD by exploring its impact on mitochondrial damage and the activation of the cGAS/STING signaling pathway. By shedding light on the involvement of TDP43 in the inflammatory activation of astrocytes in NMOSD, our study offers new insights for potential therapeutic targets in the clinical treatment of NMOSD.

Methods and materials

Reagents

TDP43 antibody (for immunofluorescence, #ab104223), antibody against translocase of outer mitochondrial membrane 20 (Tomm20, #ab186735), and Mounting Medium with DAPI (#ab104139) were purchased from Abcam (Cambridge, UK). A Pierce™ Rapid Gold BCA Protein Assay Kit (#A53225), a Melon™ Gel IgG Spin Purification Kit (#45206), AQP4 antibody (#PA5-53234), GFAP antibody (#MA5-12023), Opti-MEM™ Reduced Serum Medium (#31985070), fetal bovine serum (FBS, #A3161001C), ionized calcium-binding adapter molecule 1 (Iba1) antibody (#MA5-27726), Live Cell Imaging Solution (#A14291DJ), Lipofectamine™ RNAiMAX Transfection Reagent (#13778150), Lipofectamine™ LTX Transfection Reagent (#15338100), tetramethylrhodamine ethyl ester perchlorate (TMRE, #T669), MitoSOX™ (#M36008), Alexa Fluor™ 488 phalloidin (#A12379), and Cell Mitochondria Isolation Kit (#89874) were obtained from Thermo Fisher Scientific (Massachusetts, USA). An IL-6 detection kit (#KE10007), an IL-1 β detection kit (#KE10002), a TNF- α detection kit (#KE10003), TDP43 antibody (for western blot, #10782-2-AP), p-TDP43 antibody (Ser409/410, #22309-1-AP), cGAS antibody (for western blot, #26416-1-AP), STING antibody (for western blot, #19851-1-AP), Myelin basic protein (MBP) antibody (#10458-1-AP), inducible nitric oxide synthase (iNOS) antibody (#22226-1-AP), C3/C3b/C3c antibody (#21337-1-AP), S100A10 antibody (#11250-1-AP), Mitochondrial transcription factor A (TFAM) antibody (#22586-1-AP), and glyceraldehyde 3-phosphate dehydrogenase (GAPDH) antibody (#60004-1-Ig) were obtained from Proteintech (Wuhan, Hubei, China). STING antibody (for immunofluorescence, #13647S) and Histone H3 antibody (#4499) were obtained from CST (Massachusetts, USA). The siRNA specific for TDP43 was obtained from GenePharma Technology (Shanghai, China). AAV-GFAP-TDP43 were constructed by Packgene Technology (Guangzhou, China). The AAV-GfaABC1D-sh-TDP43 and TDP43 plasmid was constructed by OBiO Technology (Shanghai, China). AQP4 p201-220 peptides was produced by GL Biochem (Shanghai, China). RIPA buffer (#FD009), 5 \times DualColor protein loading buffer (#FD006), an FDBio-Dura ECL kit (#FD8082), Goat anti-rabbit IgG (H+L)-HRP (#FDR007), and Goat anti-mouse IgG (H+L)-HRP (#FDM007) were purchased from FDBIO SCIENCE (Hangzhou, Zhejiang, China). Goat anti-mouse IgG Dylight 549 (#A23310), Goat anti-rabbit IgG Dylight 549 (#A23320), Goat anti-mouse IgG Dylight 488 (#A23210), Goat anti-rabbit IgG Dylight 488 (#A23220) and Goat anti-rabbit IgG Dylight 649 (#A23630) were obtained from Abbkine Scientific (Wuhan, Hubei, China). Protease Inhibitor Cocktail (#CW2200S) and Phosphatase Inhibitor Cocktail

(#CW2383S) were obtained from CWBIO (Jiangsu, China). An RNA Easy Fast Tissue/Cell Kit (#DP451), FastKing gDNA Dispelling RT SuperMix (#KR118), Cell/tissue genomic DNA extraction kit (#DP304) and FastReal qPCR PreMix (SYBR Green, #FP217) were purchased from TIANGEN Biotech (Beijing, China). Nuclear protein and cytoplasmic protein extraction kit (#P0027) was purchased from Beyotime Biotech (Shanghai, China). Human complement (#S1764) and pentobarbital Sodium (#P3761) were purchased from Sigma-Aldrich (Missouri, USA). RU.521 (#S6841) and H151 (#S6652) were purchased from Selleck (Texas, USA). Human TDP43 ELISA Kit (#EK16829-96T) was purchased from SAB Biotech (South Dakota, USA). Human 2'3'-cGAMP ELISA Kit (#MM-60017H1) was purchased from MEIMIAN Biotech (Jiangsu, China). Complete Freund's adjuvant (#7027) containing mycobacterium tuberculosis (H37Ra) was purchased from Chondrex (Woodinville, WA, USA). Pertussis toxin (#GC17532) was purchased from GLP BIO (California, USA).

Mice

Eight-week-old male C57BL/6 mice were purchased from Beijing HFK Bioscience Co., Ltd (Beijing, China). The mice were raised in the experimental animal center of Southern Medical University (Guangzhou, China) under specific pathogen-free conditions. Mice could freely get water and food. The environment was well-ventilated and the relative temperature fluctuated at 22 ± 2 °C. Subsequent experiments will be conducted on mice after 5–7 days of adaptation to the animal room environment. Animal research reports comply with the NIH Guide for the Care and Use of Laboratory Animals (NIH, revised 1996) and ARRIVE guidelines 3.0. All animal experiments were approved by the Experimental Animal Ethics Committee of Southern Medical University and conducted in a blind manner, experimenters were unaware of the treatment conditions.

Collection and preparation of cerebrospinal fluid (CSF) and serum from patients

Only patients with AQP4-IgG seropositive NMOSD according to the 2015 International Panel for Neuro-myelitis Optica Diagnosis criteria were enrolled in this study [30]. Patients with negative AQP4 serology were not included in the analysis and subsequent experiments. Full informed consent was obtained from patients and the collection of CSF and serum was conducted under the approval of the Research ethics committee (Approved Number: K-2023-087-01) and performed in accordance with the ethical standards laid down in an appropriate version of the 1964 Declaration of Helsinki. All persons gave their informed consent prior to their inclusion in the study. All patients underwent lumbar puncture and

blood collection within 3 days after admission to obtain CSF and blood samples. These samples were centrifuged at 3000 rpm within 30 min. The supernatant was transferred to a sample tube and stored at -80°C for further determination. We collected the serum and CSF of a total of 8 control patients. Among them, there were 8 samples of CSF and 5 samples of serum. We collected the serum and CSF of a total of 21 NMOSD patients. Among them, there are 21 serum samples and 17 CSF samples. The content of TDP43 was not detected in the serum sample of patient #13 and the contents of TDP43 and cGAMP were not detected in the CSF sample of patient #6 (The information of the patients was shown in Supplemental Tables 1 and 2). The sample of CSF and serum were collected at the same time.

The purification of patient-derived antibody

Sera were obtained from control patients with non-inflammatory and non-autoimmune diseases, and NMOSD patients with positive AQP4-IgG serum samples. Using Melon™ Gel IgG Spin Purification Kit, we separated and purified IgG from serum samples, and concentrated the IgG concentration to 25 mg/mL with vacuum freeze dryer (LABGENE, Bjarkesvej, Denmark).

The induction of the passive and active immunization NMOSD mouse models

The passive immunization NMOSD model was established using 8-week-old male mice. Mice were anesthetized with 1% pentobarbital sodium, and a mixture of purified antibodies and 10% human complement (hC) was injected intrathecally using an insulin syringe. The tail flick indicates that the needle has successfully entered the subdural cavity of mouse. On day 0, 1, and 2, each mouse was injected with 10 μL antibody (25 mg/mL) and 10% hC mixture continuously at the same time. A series of behavioral tests were conducted on day 4, and then the spinal cord was collected for subsequent experiments.

The active immunization NMOSD model was established using 8-week-old mice. As described [31], AQP4 p201-220 peptides were emulsified in 8 mg/mL complete Freund's adjuvant (CFA) supplemented with mycobacterium tuberculosis H37Ra, the final AQP4 peptide concentration was 1 mg/mL. On day 0, mice were injected subcutaneously on the back with 200 μg of emulsion mixture. Control group mice were treated with CFA and sterile PBS. All mice were intraperitoneally injected with 200 ng pertussis toxin on day 0 and day 2. The clinical symptoms were scored at a blind manner according to the following scale: 0, no disease; 1, limp tail; 2, hind limb weakness; 3, hind limb paresis; 4, hind limb paralysis; 5, hind limb and fore limb paralysis; 6, moribundity and death. When most mice are at the peak of disease, behavioral tests were carried out.

Open field test (OFT)

Put the mice into squares ($40\times 40\times 40\text{ cm}^3$) facing the wall and let them explore the environment freely for 5 min. A video tracking software was used to record the total traveled distance and average speed, during the 5 min. Each mouse was placed in the same position. After the test of each mouse, the site was washed with 75% ethanol.

Pole test

This experiment serves as a means to assess the motor skills, coordination, and crawling abilities of the mice. Mice were trained for 3 days before formal testing and acclimated for 2 h in the testing room before the experiment. Position the mice at the top of the pole, carefully observe their crawling behavior, and meticulously record the time it takes for them to reach the bottom platform.

Rotarod test

This experiment assesses the coordinated movement, balance ability, and exercise endurance of the mice. Prior to the formal testing, the mice underwent training to acclimate them to the movements on the spinning stick. The mice were placed on a rotating stick and their performance was observed as the stick rotated at a speed of 15 rpm. The test lasted for 5 min, during which the drop time of each mouse was recorded.

Extraction of CSF from mice

Extracting CSF from mice is described as follow. Initially, the mice were anesthetized and placed in a prone position, and its head was stabilized to allow for precise access to the cisterna magna. Using aseptic techniques, the fur on the back of the neck was shaved, and the skin was cleaned to reduce the risk of contamination. A small incision was then made in the skin to expose the underlying muscles. The muscles covering the atlanto-occipital membrane were carefully dissected to reveal the cisterna magna. A fine-gauge needle, attached to a syringe, was then slowly inserted into the cisterna magna. Once the needle is correctly positioned, a small volume of CSF was gently aspirated into the syringe.

Single-nucleus library preparation and sequencing

Single-nucleus library preparation and sequencing according to our previous reports [32]. Once the extracted nuclei passed the quality test, single-nucleus RNA sequencing (snRNA-seq) libraries were prepared with Chromium Next GEM Single Cell 3' Reagent Kits v3.1 on the Chromium Controller ($10\times$ Genomics). Single-nuclei gel beads in the emulsion (GEMs) were produced as directed by the manufacturer. The released RNA of single nuclei was barcoded in each GEM via reverse transcription. Sequencing was performed with a depth

of at least half a million reads/cell and 150 bp paired-end reads (PE150) using the Illumina NovaSeq 6000.

snRNA-seq data processing

Cell Ranger (version 6.0.1) was used to align the sequencing reads to the mm10 mouse reference with default parameters, and the generated count matrix of 6 samples were input into Seurat (version 4.3.0) workflow. Firstly, cells with poor quality were removed, if (1) RNA read counts > 50,000; (2) gene numbers > 10,000; (3) mitochondrial percentage > 10. The matrix of each sample was normalized and scaled by *SCTransform* function, and then integrated into the un-batched dataset by canonical correlation analysis with normalization method as SCT.

For samples from Control and NMOSD groups, principal component analysis (PCA) was performed by *prcomp* function. FindMarkers was used to identify the differentially expressed genes (DEGs) between Control and NMOSD groups, as well as among different cell types, genes with $|\log_2\text{Fold change}| \geq 0.25$ and adjusted P value < 0.05 were regarded as significant. DEG's pathway enrichment was achieved by R package clusterProfiler (version 4.6.2) with adjusted P value < 0.05. The gene set scores in different groups were calculated by *AddModuleScore* function, and visualized via R package ggplot2 (version 3.5.1). In addition, gene set enrichment analysis (GSEA) was performed by R package GSEABase (version 1.60.0) with the fold change-ordered genes in each astrocyte subtype.

Cell culture and treatment

The preparation of mouse astrocyte was conducted as previously reported [33]. Briefly, the P1-P3 neonatal wild-type (WT) mice were sacrificed to prepare single-cell suspension from the cerebral cortex. The cells were cultured in DMEM containing 10% FBS at 37 °C and 5% CO₂ for 7 days. Shake the culture at 200 rpm for 6 h at 37 °C to collect purified microglia. After separating microglia and astrocytes in the supernatant and the bottom of the bottle, the supernatant is removed to isolate purified astrocytes. The purified astrocyte cultures are then treated with a mixed solution containing AQP4-IgG/CON-IgG (40 µg/mL) and hC (2%) for 24 h. The treated cells are then collected for western blot, RT-PCR analysis, and fluorescence staining. The human astrocyte cell line (HA) SVG p12 were cultured as previously described [34]. Briefly, SVG p12 cell line was cultured in DMEM medium containing 10% FBS at 37 °C. SVG p12 cells were passaged every four days, and the passage within five was used for experiment. The modeling method is consistent with primary astrocytes.

Drug administration

According to the manufacturer's instructions, RU.521 (cGAS inhibitor) and H151 (STING inhibitor) are sequentially dissolved in DMSO, PEG300, Tween80, and ddH₂O, ensuring clarification at each step before proceeding to the next step. The control group is a mixture of the above solvents. For inhibition of cGAS and STING, RU.521 (at a dose of 10 mg/kg) and H151 (at a dose of 5 mg/kg) were injected intraperitoneally at 1 h before NMOSD modeling. The delivery way and dosage were adopted according to previous report [35].

Knockdown of TDP43 in primary astrocytes and SVG p12 cells

Silencing of TDP43 in primary astrocytes and SVG p12 cells in vitro was achieved by transfecting si-RNA specific for TDP43. The sequences for TDP43 (human) were as follows: si-TDP43-1: "CCGGCUGGUAGAAGGAAUUTT", si-TDP43-2: "GGAUGAACUUUGGUGCGUUTT", si-TDP43-3: "GCUCAAGCAUGGAUUCUAAT T", si-TDP43-4: "GGGUGAUGUUCUAUUUACATT". The sequences for TDP43 (mouse) were as follows: si-TDP43-1: "GAACGAUGAACCCAUUGAA", si-TDP43-2: "GGUUAUUGUUGUCAACUAU", si-TDP43-3: "GAGAGGUUCUUAUGGUUCA". Scrambled si-RNA sequences were used as the negative control (NC). According to the manufacturer's instructions, NC or si-TDP43 was incubated with RNAiMAX reagent for 10 min. Then, the mixture was added to astrocytes and SVG p12 cells. After transfection, culture medium was removed and replaced with fresh medium. The cells were used for further analysis and the knockdown efficacy was verified by western blot.

Overexpression of TDP43 in primary astrocytes and SVG p12 cells

Overexpression of TDP43 was successfully induced in primary astrocytes and SVG p12 cells through transfection with TDP43 plasmid. Specifically, the TDP43 plasmid or vector was combined with LTX reagent and incubated for 10 min. The resulting mixture was then added to the astrocytes and SVG p12 cells, followed by a 12-hour transfection process. The overexpression efficacy was confirmed through western blot.

Silencing of TDP43 expression in mice

The sequence of short hairpin RNA (shRNA) targeting TDP43 (sh-TDP43) was "GGUUAUUGUUGUCAACUAU". Sh-TDP43 and the NC were cloned into pAAV-GfaABC1D-EGFP-3xFLAG-WPRE. At 3 weeks before NMOSD modeling, AAV coding NC or sh-TDP43 was injected into the vertebral canal. The knockdown efficacy was verified by western blot.

Overexpression of TDP43 in mice

TDP43-overexpressed AAV specifically transfected with astrocytes were constructed by Packgene Technology. The AAV-GFAP-hTARDBP-P2A-EGFP-WPRE-SV40pA was used, and AAV9 serotype was selected for packaging. The control group was an empty AAV containing invalid sequence. Four weeks before NMOSD modeling, AAV-TDP43 or AAV-Vector were directly injected into the vertebral canal. The overexpression efficacy was verified by western blot.

Western blot

RIPA buffer containing a mixture of 1% protease inhibitor and 1% phosphatase inhibitor was used to lyse brain tissues and cell samples. Protein concentration was detected and quantified using the BCA protein analysis kit. After boiling the protein sample in reducing loading buffer, proteins with different molecular weights were separated by 10–12.5% SDS-PAGE, and then transferred to 0.22 μ m PVDF membrane. The membrane was blocked with 5% skim milk at room temperature (RT) for 2 h, washed with TBST, and incubated primary antibody overnight at 4 °C. After washing with TBST, the membrane was incubated with HRP-conjugated secondary antibodies at RT for 1 h. Finally, after TBST cleaning, the membrane was exposed with ECL, and the immunoreactivity was detected using a chemiluminescence imager (5200, Tanon, Shanghai, China). Image J was used for detecting and analyzing grayscale values.

Immunofluorescence staining

After infusion of pre-cold PBS and 4% paraformaldehyde (PFA) into the heart, the spinal cord of the mouse was carefully removed and fixed overnight in 4% PFA at 4 °C. The samples were then dehydrated in sequential 10–30% sucrose solutions until settling at the bottom. They were then placed in OCT embedding reagent and sliced into 20- μ m-thick axial sections using a Cryostat Microtome (Leica CM1950, Nussloch, Baden Wuerttemberg, Germany). The spinal cord sections were cleaned with PBS at RT, permeated with 0.3% Triton X-100 for 30 min, and blocked with 10% goat serum for 1 h. After another round of PBS cleaning, the slices were incubated with primary antibodies overnight at 4 °C, followed by incubation with secondary antibodies for 2 h at room temperature and three PBS washes. Finally, the slices were spread flat on a slide, sealed with Fluoroshield Mounting Medium with DAPI for nuclear staining. The sections were observed using a confocal microscope (Nikon ECLIPSE Ti, Chiyoda Ward, Tokyo, Japan), and the fluorescence intensity was analyzed using Image J software.

Hematoxylin-eosin (HE) staining

The spinal cord tissue was initially fixed in 4% PFA at 4 °C for 48 h. Subsequently, it underwent a series of processes including dehydration with gradient ethanol (50–100%), clearing in xylene, and paraffin embedding. Sections of 5 μ m thickness were cut, baked at 60 °C for 2–4 h, and then deparaffinized and rehydrated. After that, the sections were stained with Harris hematoxylin for 5–10 min, differentiated, blued, and then stained with eosin for 2–5 min. Finally, they were dehydrated, cleared, and mounted with neutral balsam. The sections were scan with a scanner.

Enzyme-linked immunosorbent assay (ELISA)

The human TDP43 ELISA kit and the human 2'3'-cGAMP ELISA kit were used for detection of CSF and serum samples obtained from both control individuals and those with NMOSD. The IL-6 detection kit, IL-1 β detection kit, and TNF- α detection kit were used for detection of cytokine levels in the spinal cord. Following the manufacturer's instructions, the reagent kit was first brought to RT for 20 min to prepare a standard solution. Then, 100 μ L of the diluted standard or samples was added to each well, followed by a 2-hour incubation period at 37 °C. After aspirating the contents, 100 μ L of prepared detection reagent A was added, with an additional 1 h incubation at 37 °C. The wells were washed 3 times before adding 100 μ L of prepared detection reagent B, followed by another 1 h incubation at 37 °C. The wells were then washed 5 times before adding 90 μ L of substrate solution. This was followed by a 15–25 min incubation at 37 °C, after which 50 μ L of stop solution was added, and the OD value was immediately read at 450 nm. By establishing a standard curve, the actual concentration of the target factor was accurately calculated.

TMRE staining for mitochondrial membrane potential (MMP) detection

The variability of MMP was investigated using TMRE staining. Cells were cultured in confocal dishes overnight. After setting up the experiment, the cells were washed with PBS and then treated with 100 nM TMRE dye for 15 min before transferring to Live Cell Imaging Solution. The confocal dishes were then placed in an inverted confocal microscope for visualization. The fluorescence intensity of the images was analyzed using Image J software.

MitoSOX staining for detecting mitochondrial ROS

MitoSOX staining was utilized to assess oxidative stress in primary astrocytes. The cells were cultured in confocal dishes and subjected to modeling. Subsequently, they were treated with 500 nM MitoSOX dye for 30 min. The medium was then replaced with Live Cell Imaging

Solution. The alterations in MitoSOX fluorescence were observed using a confocal microscope and analyzed using Image J software.

Real-time quantitative PCR (RT-PCR)

For mtDNA copy number analysis, total DNA was extracted from primary astrocytes using Cell/tissue genomic DNA extraction kit. RT-PCRs were performed on LightCycler480 (Roche, Rotkreuz, Switzerland) using a 20 μ L mixture of SYBR Premix Ex Taq II Kit, DNA samples, and appropriate primers. The ratio of mitochondria DNA to nuclear DNA (mtDNA/nucDNA) was shown as relative mtDNA copy number. The primers for the Dloop2 gene were as follows: forward, 5'-CCCTTCCCC ATTTGGTCT-3'; reverse, 5'-TGGTTTCACGGAGGAT GG-3'. The primers for the 16 S gene were as follows: forward, 5'-CACTGCCTGCCAGTGA-3'; reverse, 5'-ATACCGCGGCCGTTAAA-3'. The primers for the NDUFV1 gene were as follows: forward, 5'-CTTCCCCACTGGCC TCAAG-3'; reverse, 5'-CCAAAACCCAGTGATCCAG C-3'.

F-actin staining

After the modeling process, the samples were fixed with 4% PFA, transparented with 0.3% Triton X-100, and blocked using 10% goat serum. The F-actin was stained with Alexa Fluor™ 488 phalloidin at RT for 30 min. The F-actin filaments of the cells were visualized using a confocal microscope and analyzed using Image J.

Statistical analysis

GraphPad Prism 8.3.0 (GraphPad Software, La Jolla, CA, USA) was used for statistical analysis and graph drawing. Data were expressed as the mean \pm standard deviation (SD) or mean \pm standard error of the mean (SEM). Student's t-test was used for comparisons between the two groups. One-way ANOVA (analysis of variance) followed by Tukey's post-hoc test was used for comparisons between more than two groups. $P < 0.05$ was defined as statistically significant (* $P < 0.05$; ** $P < 0.01$; *** $P < 0.001$).

Results

The level of astrocytic TDP43 is increased in both in vivo and in vitro NMOSD models

As an autoimmune inflammatory demyelinating disease, NMOSD chiefly manifests with motor impairments and sensory deficits [1]. We established the passive immunization NMOSD model by injecting AQP4-IgG and hC through intrathecal injection, and the results of GFAP, AQP4, and MBP immunostaining confirmed our model (Figure S1). A series of motor behavioral experiments were conducted to further confirm this model (Fig. 1A). The results, as illustrated in Fig. 1B and C, revealed that the NMOSD group exhibited a notably reduced average

speed ($P < 0.05$) and distance ($P < 0.05$) in the open field test (OFT). In the pole test, the NMOSD group took a significantly longer time to descend the pole (Fig. 1D, $P < 0.05$). Correspondingly, during the rotarod test, the model mice exhibited a significant decrease in the duration of sustained movement on the rotating rod (Fig. 1E, $P < 0.01$). The above data suggested that the coordination, balance, and exercise endurance of the NMOSD model mice are significantly compromised. Moreover, western blot analysis revealed a significant decrease in AQP4 expression in the spinal cord lesions of NMOSD mice (Fig. 1F and G, $P < 0.05$), which are consistent with the typical pathological characteristics observed in NMOSD patients.

Disruption in TDP43 causes neurological dysfunction [20, 21]. Our study revealed a significant upregulation of TDP43 expression in the spinal cord lesions of NMOSD mice (Fig. 1F and H, $P < 0.05$). Meanwhile, we also found an upregulation of p-TDP43 (Ser409/410) in the spinal cord of NMOSD mice (Figure S2, $P < 0.05$). Subsequently, we examined the TDP43 expression of astrocytes in the spinal cord using immunostaining. The results shown in Fig. 1I demonstrate a marked increase in astrocytic TDP43 expression in NMOSD model mice compared to the control group. Then, we explored the change of astrocytic TDP43 in the NMOSD cell model. Consistent with in vivo results, AQP4-IgG purified from NMOSD patients caused decreased protein levels of AQP4 (Fig. 1K and L, $P < 0.01$) and an increased expression of TDP43 (Fig. 1K and M, $P < 0.01$). At the same time, we also detected the translocation of TDP43 in astrocytes. As shown in Fig. 1N–P, AQP4-IgG caused increased TDP43 level in the cytoplasm ($P < 0.01$), which suggested the translocation of TDP43 from nucleus to cytoplasm. Overall, these findings indicate an abnormal elevation in astrocytic TDP43 expression in NMOSD.

NMOSD induces A1-like reactive astrocytes

To delve deeper into the variance of astrocytes in NMOSD, we firstly established NMOSD mice model according to our previous report [36]. The lesion of striatum was shown in Figure S3. We collected tissue from the lesion site of NMOSD mice and conducted snRNA-seq. After quality control, we obtained 52,073 cells ($n = 23,545$ in Control, $n = 28,528$ in NMOSD group) to identify 8 cell types according to the canonical cell markers (Figure S4A–B), including neuron (*Neurod6+*), oligodendrocyte (*Olig1+*), oligodendrocyte precursor cell (*Vcan+*), astrocyte (*Gfap+*), microglia (*Aif1+*), endothelia (*Pecam1+*), ependymal cell (*Pifo+*), and fibroblast (*Col1a2+*). Among these cell types, neuron accounted the most abundance ($n = 28,281$ (54.31%), Figure S4C), followed by microglia ($n = 8,440$ (16.21%)). Data showed unbatched between Control and NMOSD groups (Figure

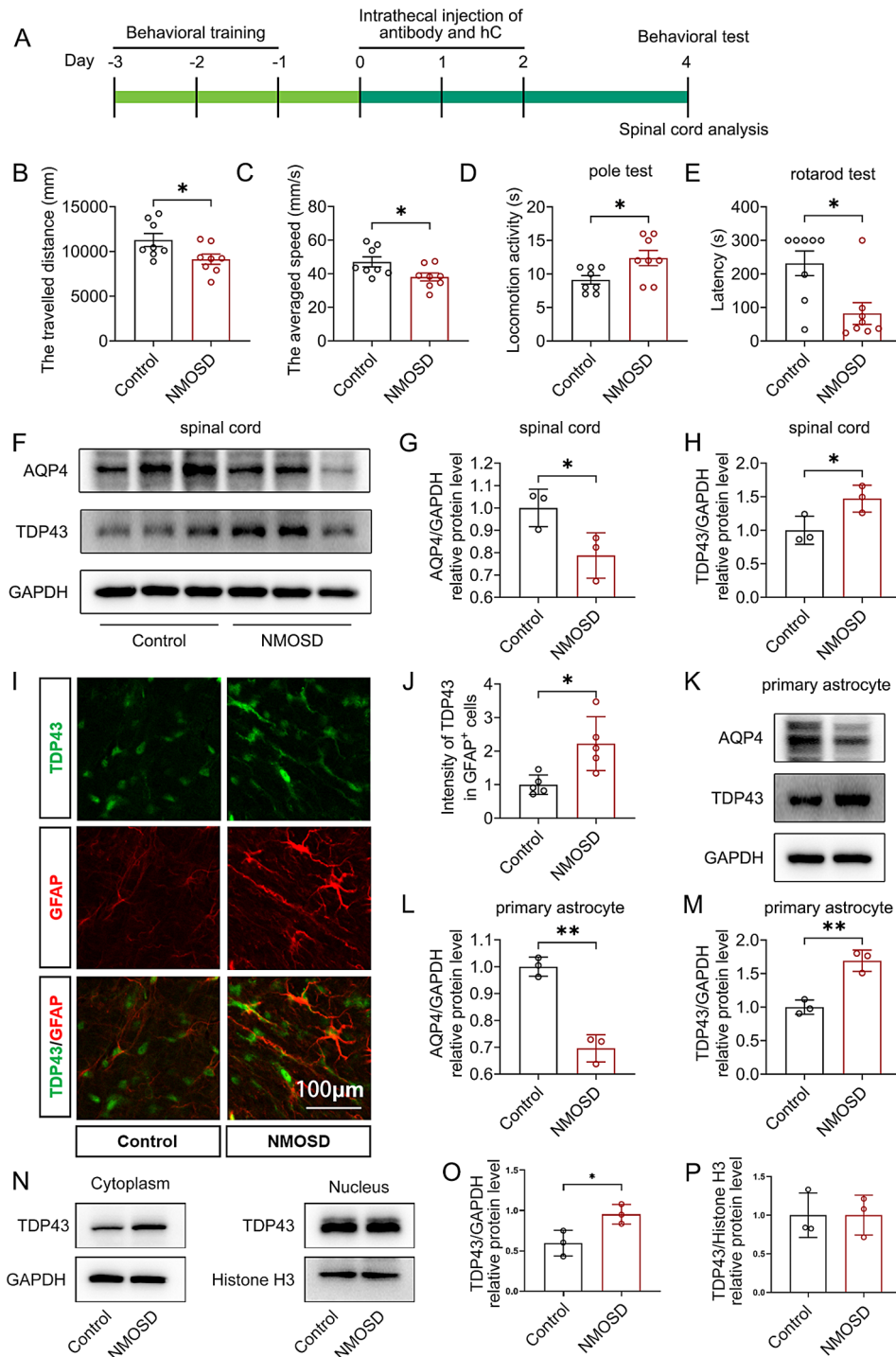


Fig. 1 The level of astrocytic TDP43 is increased in NMOSD models. **(A)** The schedule shows details of the experiment. **(B and C)** The control group and passive immunization NMOSD model mice were assessed in the open field for the averaged speed and the travelled distance ($n=8$). **(D)** The mice were assessed in the pole test for the time spent climbing down ($n=8$). **(E)** The mice were assessed in the rotarod test for the maintenance time on the rotating stick ($n=8$). After the behavioral test, the mice were sacrificed and the spinal cord was quickly collected. **(F–H)** The changes of AQP4 and TDP43 were determined by western blot and quantified using Image J ($n=3$). **(I and J)** The variance of TDP43 in astrocytes of the spinal cord was visualized by double-staining with GFAP and TDP43 and quantified using Image J ($n=5$). Scale bar: 100 μm. **(K–M)** Primary astrocytes were exposed to AQP4-IgG (40 μg/mL) and hC (2%) for 24 h, then the variance of TDP43 and AQP4 were determined by western blot ($n=3$). **(N–P)** Primary astrocytes were exposed to AQP4-IgG and hC for 24 h, then the variance of TDP43 in the cytoplasm and nucleus were determined by western blot ($n=3$). Behavioral test results are expressed as the mean \pm SEM, and other results are expressed as the mean \pm SD, * $P < 0.05$, ** $P < 0.01$, *** $P < 0.001$ versus the indicated group

S4D). Compared to the Control group, NMOSD harbored less neuron, oligodendrocyte, astrocyte, as well as more oligodendrocyte precursor Cell, microglia and endothelia cells (Figure S4E).

To delve deeper into the variance of astrocytes in NMOSD, we subset astrocytes to perform further re-clustering. Principal component analysis revealed that NMOSD mice samples cluster separately from control samples as expected (Figure S4F). Differential gene-expression analysis contrasting NMOSD mice with the control group yielded 4381 DEGs in astrocytes (4324 up-regulated and 57 down-regulated, Fig. 2A), which exhibited good consistency among different samples in the NMOSD and control groups (Figure S4G). Our sequencing results confirmed the transcriptional elevation of TDP43 in astrocytes (Fig. 2A). Pathway enrichment analysis revealed functional differences between up- and down-regulated terms (Fig. 2B). The up-regulated DEGs participated in DNA damage stimulus response, mRNA surveillance pathway, and glutamatergic synapse, and down-regulated DEGs were associated with reactive oxygen species, oxidative phosphorylation, and neurodegeneration pathways. Based on the expressions of canonical markers (Figure S4H), we distinguished 7 major astrocyte types (Fig. 2C), including C1 (*Mertk*+), C2 (*Mir99ahg*+), C3 (*Pde10a*+), C4 (*Apoe*+), C5 (*Adarb2*+), C6 (*Top2a*+), and C7 (*Pde4b*+). The relative expression levels of cluster-specific genes (Figure S4I) revealed the distinct transcriptomic programs across the different subtypes, regulating the respective biological processes (Fig. 2D), such as glutamatergic synapse in *Mertk*+ C1 and glial cell fate commitment in *Mir99ahg*+ C2 cells. To elucidate the role of astrocytes in the pathology of NMOSD, we evaluated the scores of known transcriptomic signatures in pan-reactive, A1-like, and A2-like astrocytes (Fig. 2E). The sequencing results revealed that NMOSD induced significant changes in astrocyte heterogeneity and promoted A1-like activation, as evidenced by an increase in the transcription levels of *Ggta1*, *C3*, *IL-1 β* , and others (Fig. 2F). This inflammatory A1-like activation of astrocytes phenotype was further confirmed by western blot, *in vivo* results (Fig. 2G) showed an increased expression of *iNOS* (Fig. 2H, $P < 0.05$) and *C3* (Fig. 2I, $P < 0.05$), along with a decreased expression of A2-like phenotype astrocytic marker *S100A10* (Fig. 2J, $P < 0.05$). We also confirmed our results by double immunostaining *C3*/GFAP and *iNOS*/*Iba1* (Figure S5). As shown in Fig. 2K–N, AQP4-IgG purified from NMOSD patients caused consistently primary astrocyte inflammatory activation. Collectively, these data suggest that astrocytes of NMOSD mice exhibit an A1-like reactive profile.

NMOSD causes mitochondrial dysfunction and accumulation of TDP43 in astrocytic mitochondria

Prevailing studies link TDP43's mislocalization into mitochondria with mitochondrial dysfunction [22, 23]. However, the roles of TDP43 and mitochondrial dysfunction in NMOSD remain unknown. SnRNA-seq data from animal models displayed a general downtrend among mitochondria-associated genes in all 7 astrocyte types via GSEA (Fig. 3A–H), which indicates that NMOSD causes mitochondrial damage. TFAM is essential for maintaining mtDNA stability and regulating mitochondrial function [37]. Perturbed mitochondrial integrity can lead to aberrant expression levels of TFAM. Our western blot results demonstrated a significant decrease in TFAM expression levels in *in vivo* (Fig. 3I and J, $P < 0.05$) and *in vitro* (Fig. 3K and L, $P < 0.05$) models of NMOSD. Additionally, TMRE staining revealed a notable decline in mitochondrial membrane potential (MMP) in the model group (Fig. 3M and N, $P < 0.001$). With mitochondria being principal ROS sources, we investigated mitochondrial ROS alterations using MitoSOX staining. Figure 3O and P revealed an intensified mitochondrial ROS accumulation in the NMOSD group ($P < 0.001$). Given the detrimental implications of mitochondrial disruption, which is critically implicated in NMOSD's etiology and TDP43's abnormal aggregations that cause mitochondrial damage, we examined the subcellular localization changes of TDP43. Both western blot (Fig. 3Q, $P < 0.05$) and immunostaining results (Fig. 3S) demonstrated a significant mitochondrial TDP43 enrichment following incubation with AQP4-IgG *in vitro*. These findings suggested that TDP43 might be detrimental to mitochondrial integrity in NMOSD.

TDP43 aggravates mitochondrial damage and upregulates the cGAS/STING pathway in astrocytes caused by AQP4-IgG

As a subset of TDP43 proteinopathies, mtDNA releases into the cytoplasm through mitochondrial permeability transition pores and activates the cGAS/STING signaling pathway in ALS [38]. However, the role of TDP43 in NMOSD remains unknown. Therefore, we investigated whether the abnormal distribution of TDP43 in NMOSD affects mitochondrial function and cGAS/STING signaling pathways. In Figure S6A and B, our results indicated a significant increase in the level of mtDNA in the cytoplasm of primary astrocytes following AQP4-IgG stimulation. Specifically, mtDNA levels are represented by *Dloop2* (Figure S6A, $P < 0.05$) and *16 S* (Figure S6B, $P < 0.01$), with nuclear DNA *NDUFV1* as the reference gene. Additionally, the expression of cGAS (Figure S6C and D, $P < 0.001$) and STING (Figure S6C and E, $P < 0.01$) in astrocytes were significantly elevated after AQP4-IgG stimulation. Meanwhile, our *in vivo* results also

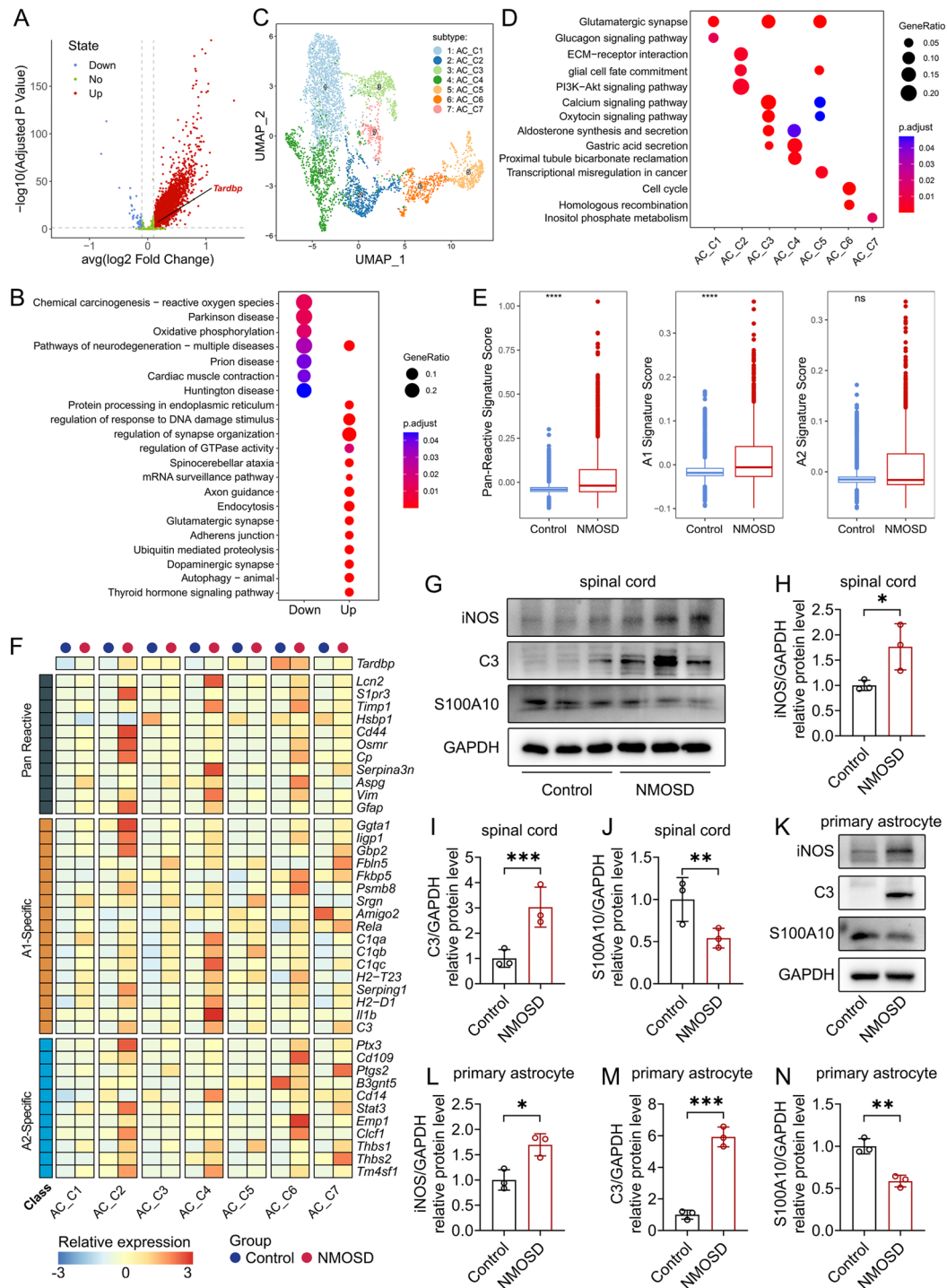


Fig. 2 NMOSD induces A1-like reactive astrocytes in mice. C57 mice were injected with an antibody and complement mixture, then the striatum was collected. Single-nucleus RNA sequencing was conducted to determine variant genes in astrocytes. **(A)** The volcano plot revealed the differentially expressed genes in astrocytes (4324 up-regulated and 57 Down-regulated). **(B)** Pathway enrichment analysis revealed the up- and down-regulated pathway in astrocytes. **(C)** Seven major astrocyte types were verified based on the expressions of canonical markers. **(D)** The respective biological processes of each astrocyte type. **(E)** The scores of transcriptomic signatures in pan-reactive, A1-like, and A2-like astrocytes of the control and NMOSD groups. **(F)** Heat map revealed the pan-reactive, A1-like, and A2-like differential expression genes between the control and NMOSD groups. C57 mice were intrathecally injected with AQP4-IgG and hC mixture continuously for 3 days. Then, the spinal cord was quickly collected on day 4. **(G–J)** The changes of iNOS, C3, and S100A10 were determined by western blot and quantified using Image J ($n=3$). **(K–N)** Primary astrocytes were exposed to purified AQP4-IgG (40 $\mu\text{g}/\text{mL}$) and hC (2%) for 24 h, then the variance of iNOS, C3, and S100A10 were determined by western blot ($n=3$). Results are expressed as the mean \pm SD, * $P < 0.05$, ** $P < 0.01$, *** $P < 0.001$ versus the indicated group

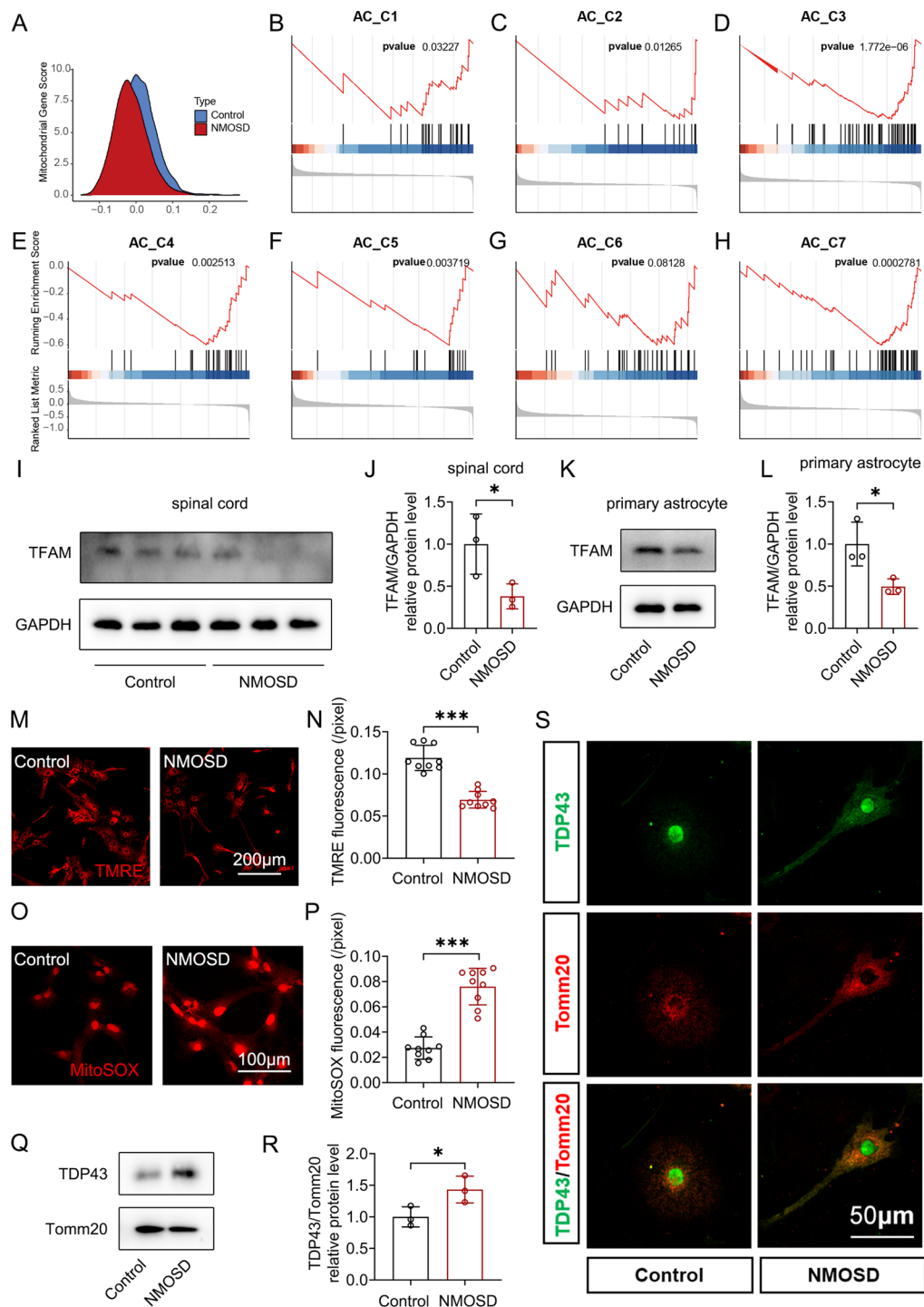


Fig. 3 NMOSD causes mitochondrial dysfunction and accumulation of TDP43 in astrocytic mitochondria. **(A–H)** Single-nucleus RNA sequencing from animal models showed a general downtrend among mitochondria-associated genes in all 7 astrocyte types. **(I and J)** The change of TFAM in the spinal cord of passive immunization NMOSD model was determined by western blot and quantified using Image J ($n=3$). Primary astrocytes were exposed to purified AQP4-IgG (40 $\mu\text{g}/\text{mL}$) and hC (2%) for 24 h. **(K and L)** The variance of TFAM was determined by western blot and quantified using Image J ($n=3$). **(M and N)** The change of mitochondrial membrane potential (MMP) in astrocytes was detected by TMRE staining ($n=3$). Scale bar: 200 μm . **(O and P)** The change of mitochondrial ROS in astrocytes was determined by MitoSOX staining ($n=3$). Scale bar: 100 μm . **(Q–S)** Abnormal accumulation of TDP43 in mitochondria of astrocytes was determined by western blot ($n=3$) and visualized with immunofluorescence. Results are expressed as the mean \pm SD, $*P<0.05$, $**P<0.01$, $***P<0.001$ versus the indicated group

confirmed the upgradation of the cGAS/STING pathway in NMOSD mice (Figure S7).

A siRNA specific for TDP43 was utilized to down-regulate the expression of TDP43 in astrocytes in vitro. The knockdown efficacy was assessed using western blot (Fig. 4A). TMRE and MitoSOX staining revealed that knockdown of TDP43 mitigated the reduction of MMP (Fig. 4B and C, $P < 0.001$) and the accumulation of mitochondrial-derived ROS (Fig. 4D and E, $P < 0.05$) after AQP4-IgG stimulation. As depicted in Fig. 4F, the silence of TDP43 inhibited the release of mtDNA into the cytoplasm ($P < 0.05$) and suppressed the elevation of cGAS (Fig. 4G and H, $P < 0.05$) and STING (Fig. 4G and I, $P < 0.05$). F-actin staining showed that TDP43-knockdown mitigated astrocyte cytoskeleton damage after AQP4-IgG stimulation (Figure S8A). Additionally, as illustrated in Fig. 4J, the heightened protein expression levels of iNOS (Fig. 4K, $P < 0.05$) and the diminished protein expression levels of S100A10 (Fig. 4L, $P < 0.01$) in the model group were reversed upon TDP43-knockdown.

Then, we detected the effect of TDP43 overexpression in astrocytes. Firstly, the efficacy of overexpression was confirmed by western blot (Fig. 4M and N, $P < 0.01$). As shown in Fig. 4O, overexpression of TDP43 further reduced the MMP in model astrocytes ($P < 0.05$). We found that overexpression of TDP43 exacerbated the elevation in the level of cGAS ($P < 0.05$), STING ($P < 0.05$), and C3 ($P < 0.05$) after AQP4-IgG stimulation. The F-actin staining showed that TDP43 overexpression aggravated astrocytic cytoskeleton damage caused by the NMOSD model (Figure S8B). Overall, these results indicated that TDP43 exacerbates AQP4-IgG-induced mitochondrial damage, upregulated cGAS/STING signaling pathway, and inflammatory activation in astrocytes. Finally, as shown in Figure S9, knockdown of TDP43 mitigated the reduction of MMP in SVG p12 cells after AQP4-IgG stimulation, while overexpression of TDP43 exacerbates the reduction of MMP. Our results confirmed that TDP43 aggravated NMOSD-induced astrocytic mitochondrial dysfunction.

Astrocytic TDP43 exacerbates the severity of the NMOSD mouse model

To delve into the protective role of TDP43-knockdown in vivo, we silenced the astrocytic expression of TDP43 in the spinal cord by administering AAV-GfaABC1D-shTDP43 through intrathecal injection. The experimental schedule is shown in Fig. 5A. Our investigations confirmed that this AAV only efficiently targeted astrocytes in the spinal cord and effectively silenced TDP43 in the spinal cord by western blot analysis (Fig. 5B and C, $P < 0.01$) and immunofluorescence staining (Fig. 5D and Figure S10). Following three weeks of AAV-GfaABC1D-shTDP43 injection, we induced the passive immunization

NMOSD mouse model. The results in Fig. 5E–F demonstrated that TDP43-knockdown in the spinal cord significantly rescued the decreased speed ($P < 0.01$) and distance ($P < 0.01$) in NMOSD model mice. Furthermore, TDP43-knockdown alleviated the extended climbing time (Fig. 5G, $P < 0.05$) and enhanced the duration of sustained movement on the rotary stick in model mice (Fig. 5H, $P < 0.01$). Then, we assessed the impact of TDP43 knockdown in the spinal cord on pathological changes related to NMOSD. In alignment with in vitro findings, TDP43-knockdown in astrocyte rescued NMOSD-induced inflammatory activation of astrocytes, as evidenced by diminishing elevation in C3 (Fig. 5I and J, $P < 0.01$), GFAP (Figure S11A and B, $P < 0.01$), and STING (Figure S12A), and raising protein levels of AQP4 (Fig. 5I and K, $P < 0.01$). At the same time, we also found that TDP43-knockdown in astrocyte reduced the levels of IL-6 ($P < 0.05$), IL-1 β ($P < 0.05$), and TNF- α ($P < 0.05$) in the spinal cord (Figure S13). These results indicate that TDP43-knockdown mitigates NMOSD-induced inflammatory activation of astrocytes in vivo.

Subsequently, we investigated the impact of astrocytic TDP43 overexpression in the NMOSD model. The experimental schedule was shown in Fig. 5L. Initially, our investigations confirmed that administering AAV-GFAP-TDP43 through intrathecal injection only efficiently targeted astrocytes in the spinal cord and effectively overexpressed astrocytic TDP43 in the spinal cord by western blot analysis (Fig. 5M and N, $P < 0.05$) and immunofluorescence staining (Fig. 5O and Figure S10). Following 4-weeks of AAV-GFAP-TDP43 administration, we induced the NMOSD mouse model and assessed motor function changes in each group. The results revealed that TDP43 upregulation in the spinal cord exacerbated the decrease in speed (Fig. 5P, $P < 0.05$), distance (Fig. 5Q, $P < 0.05$), and duration on the rotary stick (Fig. 5S, $P < 0.01$) in NMOSD model mice. Additionally, the time taken for climbing in the pole test was further prolonged in the AAV-GFAP-TDP43 transfected group (Fig. 5R, $P < 0.001$). Furthermore, we assessed the impact of TDP43 on the inflammatory activation of astrocytes. TDP43 overexpression in the spinal cord worsened the increased levels in C3 (Fig. 5T and U, $P < 0.05$), GFAP (Figure S11C and D, $P < 0.05$) and STING (Figure S12B), and decreased protein level in AQP4 (Fig. 5T and V, $P < 0.01$). In summary, our data indicates that TDP43 exacerbates NMOSD-induced movement disorders and inflammatory activation of astrocytes.

Application of cGAS and STING inhibitors alleviate injury in NMOSD mice

Our data also demonstrates that TDP43 plays a role in upgrading the astrocytic cGAS/STING signaling pathway after NMOSD. To further investigate the role of cGAS/

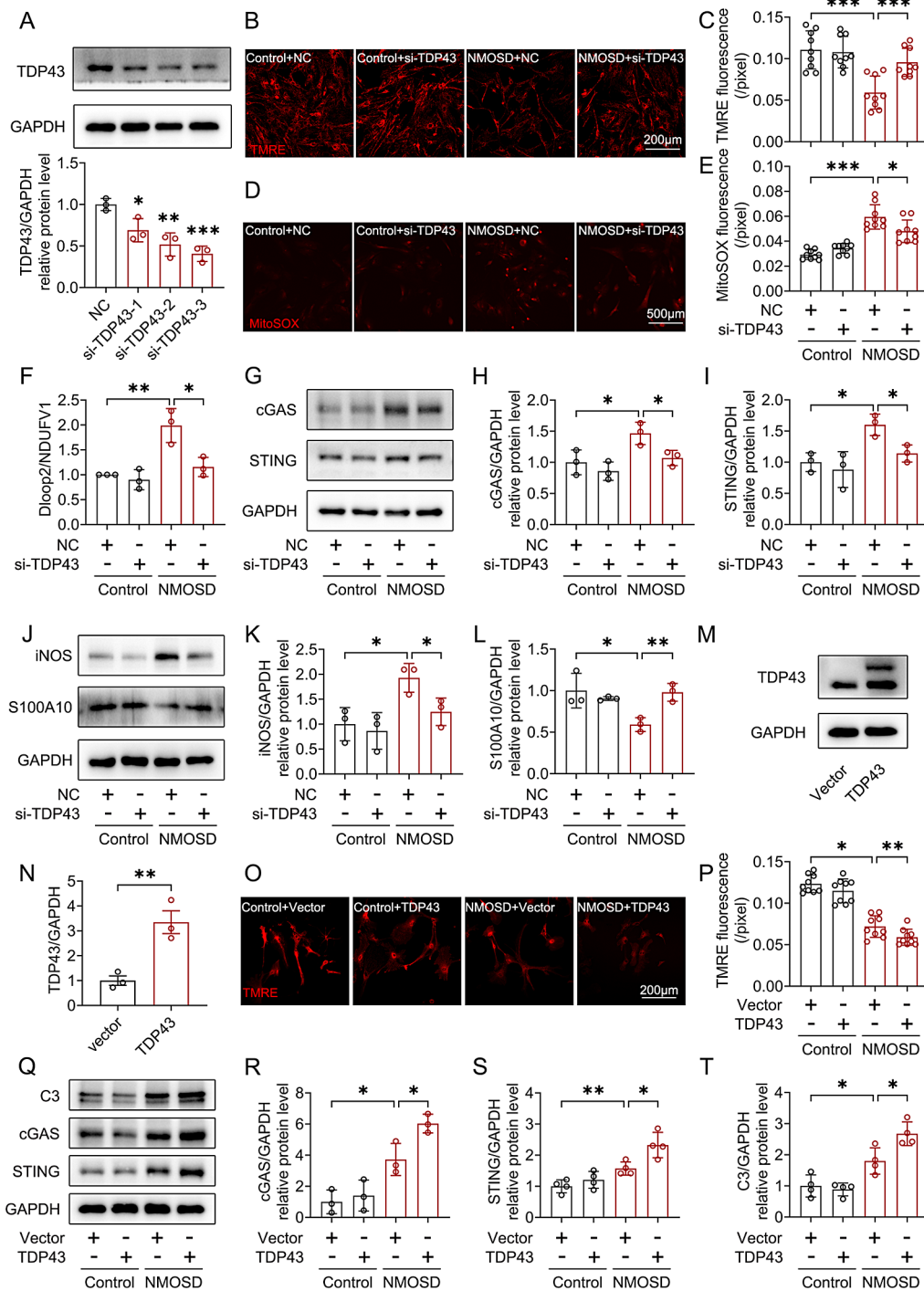


Fig. 4 TDP43 aggravates astrocyte mitochondrial damage and activation of the cGAS/STING pathway. **(A)** The knockdown efficacy of si-TDP43 was detected by western blot ($n=3$). Subsequent experiments used si-TDP43-3. Astrocytes were transfected with NC or si-TDP43, and then exposed to purified AQP4-IgG (40 μg/mL) and hC (2%) for 24 h. **(B and C)** The change of MMP was detected by TMRE staining ($n=3$). Scale bar: 200 μm. **(D and E)** The change of mitochondrial ROS in astrocytes was determined by MitoSOX staining ($n=3$). Scale bar: 500 μm. **(F)** Relative mtDNA copy number in the astrocyte NMOSD model was shown as Dloop2/NDUFV1 by RT-PCR ($n=3$). **(G-I)** The variance of cGAS and STING was detected by western blot ($n=3$). **(J-L)** The variance of iNOS, C3, and S100A10 were detected by western blot ($n=3$). **(M and N)** Astrocytes were transfected with Vector or TDP43 plasmid for 24 h, the overexpression efficacy was detected by western blot and the relative expression of TDP43/GAPDH was measured by densitometry of the blot ($n=3$). **(O and P)** The change of MMP was detected by TMRE staining ($n=3$). Scale bar: 200 μm. **(Q-T)** The variance of cGAS, STING, and C3 were detected by western blot ($n=3$). Results are expressed as the mean \pm SD, * $P < 0.05$, ** $P < 0.01$, *** $P < 0.001$ versus the indicated group

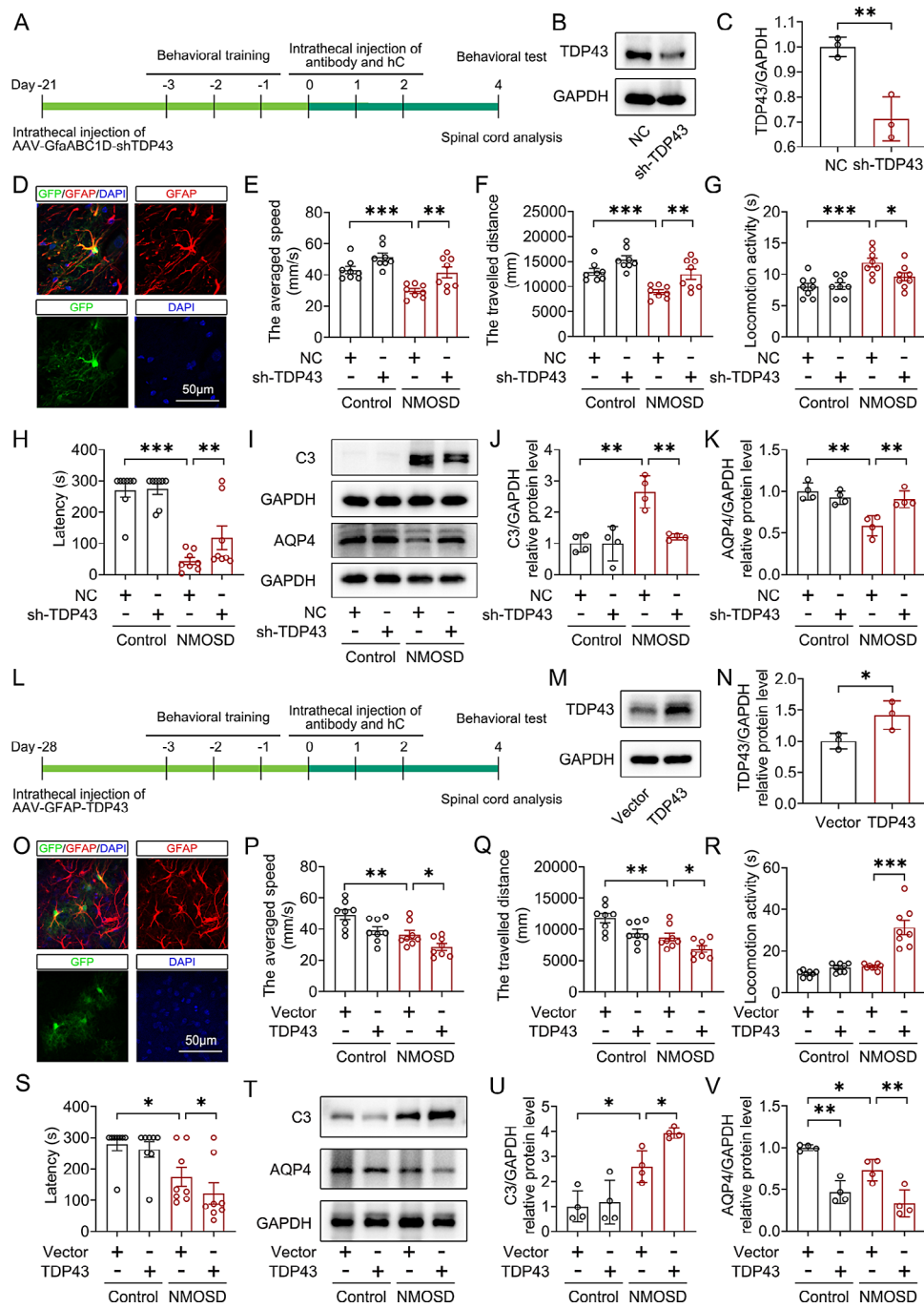


Fig. 5 TDP43 exacerbates NMOSD-induced injury in mice. **(A)** The experiment schedule shows details of silencing TDP43 in vivo. **(B and C)** C57BL/6J mice were intrathecally injected with AAV-GfaABC1D-NC or AAV-GfaABC1D-sh-TDP43, then the knockdown efficacy in the spinal cord was verified by western blot ($n=3$). **(D)** The immunofluorescence results confirmed that AAV-GfaABC1D-sh-TDP43 transfected with GFAP-positive cells in the spinal cord. **(E and F)** Mice were assessed in the open field for the average speed and the travelled distance ($n=8$). **(G)** Mice were assessed in the pole test for the time spent climbing down ($n=8$). **(H)** Mice were assessed in the rotarod test for the maintenance time on the rotating stick ($n=8$). **(I–K)** Mice were sacrificed after behavioral tests, and the spinal cord was quickly collected. The changes of AQP4 and C3 were determined by western blot ($n=3$). **(L)** The experiment schedule shows details of silencing TDP43 in vivo. **(M and N)** C57BL/6J mice were intrathecally injected with AAV-GFAP-vector or AAV-GFAP-TDP43, then the overexpression efficacy in the spinal cord was verified by western blot ($n=3$). **(O)** The immunofluorescence results confirmed that AAV-GFAP-TDP43 transfected with GFAP-positive cells in the spinal cord. **(P and Q)** Mice were assessed in the open field for the average speed and the travelled distance ($n=8$). **(R)** Mice were assessed in the pole test for the time spent climbing ($n=8$). **(S)** Mice were assessed in the rotarod test for the maintenance time on the rotating stick ($n=8$). **(T–V)** Mice were sacrificed after behavioral tests, and the spinal cord was quickly collected. The changes in AQP4 and C3 were determined by western blot ($n=4$). Behavioral test results are expressed as the mean \pm SEM, and other results are expressed as the mean \pm SD, * $P < 0.05$, ** $P < 0.01$, *** $P < 0.001$ versus the indicated group

STING signaling in NMOSD, we administered RU.521 (a cGAS inhibitor) and H151 (a STING inhibitor) in passive immunization NMOSD mice. The experimental schedule is shown in Fig. 6A. Results showed that administration of H151 (Fig. 6B and C, $P < 0.01$) or RU.521 (Fig. 6B

and C, $P < 0.001$) improved the behavioral abnormalities in NMOSD mice (Fig. 6B–E). These findings suggested that RU.521 and H151 can enhance the impaired motor ability in NMOSD mice. Results of MBP immunostaining showed that treatment with RU.521 and H151

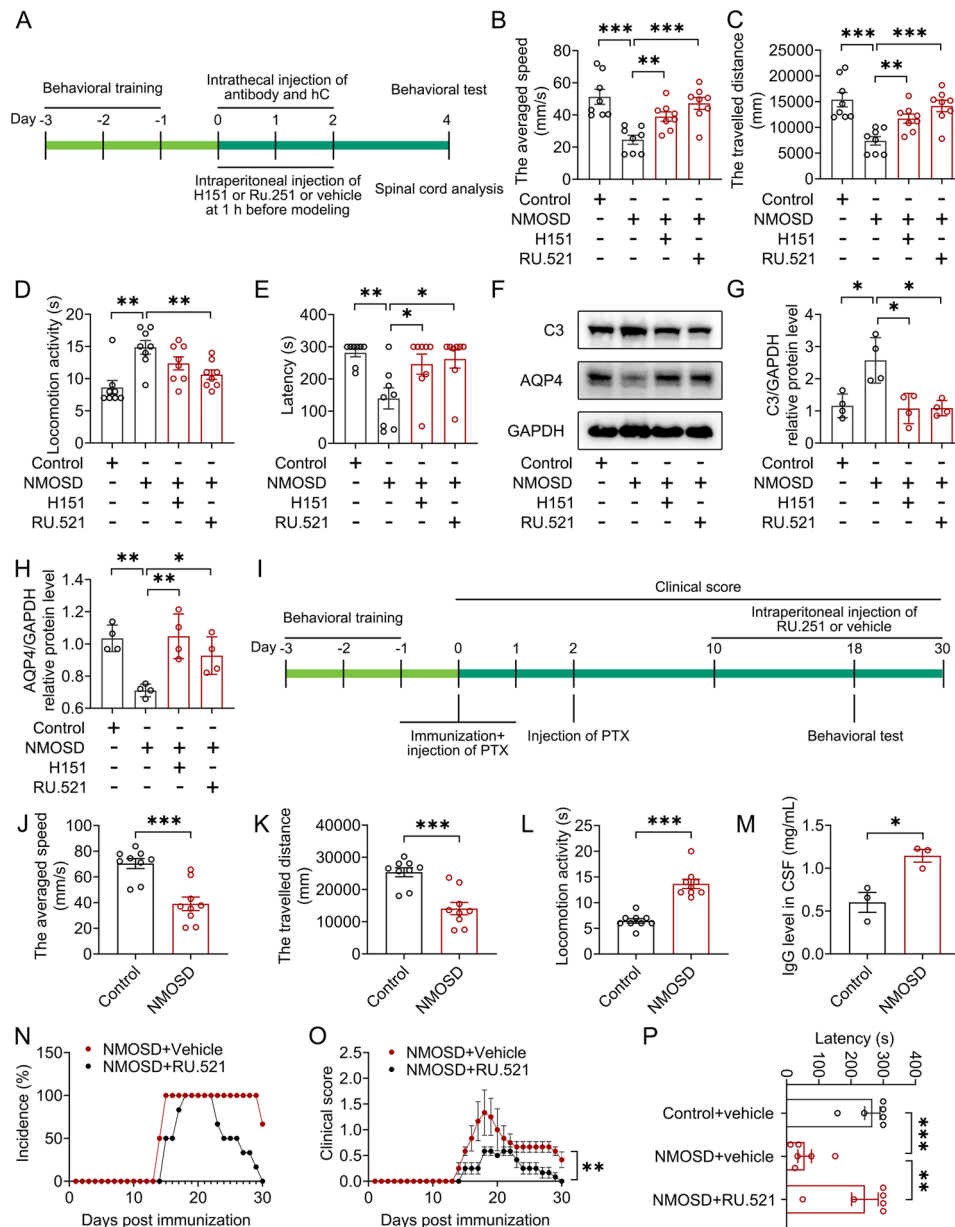


Fig. 6 Application of H151 and RU.521 alleviates NMOSD-induced injury in mice. **(A)** The experiment schedule shows details of the application of H151 and RU.521 in mice. **(B and C)** Each group of mice was assessed in the open field for the average speed and the travelled distance during a 5 min trial ($n=8$). **(D)** Each group of mice was assessed in the pole test for the time spent climbing ($n=8$). **(E)** Each group of mice was assessed in the rotarod test for the maintenance time on the rotating stick during a 5-min trial ($n=8$). Mice were sacrificed after behavioral tests, and the spinal cord was quickly collected. **(F–H)** The changes of AQP4 and C3 were determined by western blot ($n=4$). **(I)** The experiment schedule shows details of the application of RU.521 in alleviating in active immunization NMOSD mouse model. **(J and K)** Each group of mice was assessed in the open field for the average speed and the travelled distance during a 5 min trial ($n=6$). **(L)** Each group of mice was assessed in the pole test for the time spent climbing ($n=6$). **(M)** The IgG concentration of CSF in active immunization NMOSD mouse model ($n=3$). **(N)** Incidence rate within 30 days of modeling in each group ($n=6$). **(O)** The clinical score within 30 days of modeling in each group ($n=6$). **(P)** Each group of mice was assessed in the rotarod test for the maintenance time on the rotating stick during a 5-min trial. ($n=6$). Behavioral test results are expressed as the mean \pm SEM, and other results are expressed as the mean \pm SD, * $P < 0.05$, ** $P < 0.01$, *** $P < 0.001$ versus the indicated group

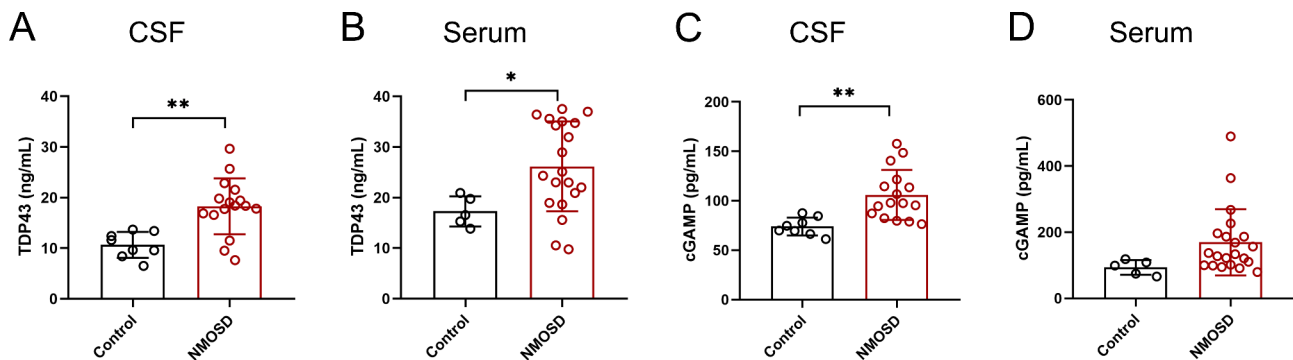


Fig. 7 The concentrations of TDP43 and cGAMP increase in CSF and serum samples of NMOSD patients. **(A)** The concentrations of TDP43 in the cerebrospinal fluid of NMOSD patients ($n=16$) and control group ($n=8$). **(B)** The concentrations of TDP43 in the serum of NMOSD patients ($n=20$) and control group ($n=5$). **(C)** The concentrations of cGAMP in the CSF of NMOSD patients ($n=16$) and control group ($n=8$). **(D)** The concentrations of cGAMP in the serum of NMOSD patients ($n=21$) and control group ($n=5$). Results are expressed as the mean \pm SD, * $P < 0.05$, ** $P < 0.01$ versus the indicated group

significantly reduced the levels of demyelination caused by NMOSD (Figure S15A and B, $P < 0.01$). HE staining showed that compared to the NMOSD group, the tissue structure in the treated group was more intact (Figure S15C). Additionally, western blot analysis showed that both H151 and RU.521 were able to decrease the upregulation of C3 (Fig. 6F and G, $P < 0.05$) and restore the loss of AQP4 (Fig. 6F and H). Immunofluorescence further confirmed that both H151 and RU.521 were able to attenuate activation of astrocytes, as evidenced by reducing GFAP levels (Figure S14, $P < 0.01$). Then, an active immunization NMOSD mouse model was established, and the experimental schedule is shown in Fig. 6I. The success in the establishment of active immunization NMOSD mouse model was confirmed by motor functional test (Fig. 6K–L, $P < 0.001$) and CSF IgG detection (Fig. 6M, $P < 0.05$). Our results further showed that administration of RU.521 shortened the pathological processes and clinical score of NMOSD mice (Fig. 6N and O, $P < 0.01$). Meanwhile, we also found that RU.521 attenuated motor dysfunction in the active immunization NMOSD mouse model, as evidenced by increasing the movement time of the model mice on the rotating rod (Fig. 6P, $P < 0.01$). We confirmed the pathological improvement in treated group in the active immunization NMOSD mouse model by MBP immunostaining (Figure S15D, $P < 0.01$) and HE staining (Figure S15F). Overall, the cGAS/STING pathway inhibitors RU.521 and H151 attenuate NMOSD-caused injury in vivo.

TDP43 and cGAMP concentrations are increased in NMOSD CSF and serum

To further validate the aforementioned in vivo findings, we collected CSF and serum samples from control group individuals and NMOSD patients. These samples were subjected to ELISA analysis. The results revealed a significant increase in TDP43 levels in both the CSF (Fig. 7A, $P < 0.01$) and serum (Fig. 7B, $P < 0.05$) of NMOSD patients

compared to the control group. Meanwhile, we also analyzed the correlation between TDP43 expression levels and EDSS scores of NMOSD patient. Our results showed that TDP43 levels in the CSF (Figure S16A, $P < 0.0001$) and serum (Figure S16B, $P < 0.001$) were positive correlated with disease severity. Moreover, cGAMP, a downstream metabolite of cGAS, can bind and activate the adapter protein STING [39]. Our results also demonstrated significantly higher levels of cGAMP in the CSF ($P < 0.01$) and serum of NMOSD patients. These findings further illustrate the crucial role of the TDP43 and cGAS/STING pathway in the pathogenesis of NMOSD.

Discussion

Our comprehensive study across both in vitro and in vivo NMOSD models unveiled a pronounced elevation in TDP43 expression levels within astrocytes. Intriguingly, silencing TDP43 alleviated mitochondrial dysfunctions, tempered inflammatory responses, and mitigated activation of the cGAS/STING signaling pathway in primary astrocytes following exposure to AQP4-IgG. Conversely, overexpression of TDP43 intensified these pathogenic alterations induced by AQP4-IgG. In a mouse model of passive immunization, knockdown of astrocytic TDP43 mitigated damages observed in model mice, while overexpression of TDP43 in astrocytes exacerbated the injury. Notably, the application of cGAS/STING signaling inhibitors, namely RU.521 and H151, ameliorated movement disorders in both passive and active immunization models. Our investigations further found elevated levels of TDP43 and cGAMP within CSF and serum samples from NMOSD patients, corroborating the pathological relevance of our findings. Summarily, our data cast light on the deleterious interplay between TDP43 abnormalities and subsequent activation of the cGAS/STING pathway in the pathogenesis of NMOSD, marking a pioneering exploration into this nexus. This study posits the TDP43/cGAS/STING axis as a pivotal contributor to NMOSD

pathology, suggesting novel therapeutic vistas for intervention in NMOSD treatment.

The conventional approach to develop an NMOSD mouse model often involves intracerebral administration of AQP4-IgG [40]. However, this method has limits in replicating the spinal cord injury in the pathological progression of NMOSD. Our preceding findings highlighted that the intrathecal injection of AQP4-IgG and complement infusion leads to a notable reduction of AQP4 expression in the spinal cord [36]. Our current research innovatively demonstrates that this model effectively precipitates motor dysfunctions in mice, a hallmark of NMOSD symptomatology. This result marks a pioneering stride towards enhancing the authenticity of the mouse model in mirroring the neurological impairments of NMOSD. This advancement sets the stage for more accurate evaluations of therapeutic approaches aimed at mitigating spinal cord involvement in NMOSD. However, it has to point out that our model employed does not fully capture the chronic nature of human NMOSD. The acute passive immunization used in our model has limitations when it comes to replicating the complex and long-term pathology seen in human patients. One must recognize that human NMOSD is a chronic disease with a diverse range of manifestations and progression patterns. In contrast, the acute nature of the mouse model may only provide insights into the initial stages of the disease process or specific acute inflammatory responses. This limitation could potentially lead to an incomplete understanding of the long-term mechanisms underlying astrocyte dysfunction and disease progression. To address this limitation, future studies could explore the use of chronic mouse models. Chronic models may better mimic the slow progression and long-term consequences of NMOSD, allowing for a more comprehensive investigation of disease mechanisms.

NMOSD is distinctly marked by the presence of AQP4-IgG in both the serum and CSF [41]. When AQP4-IgG interacts with astrocytes, it causes significant cellular damage, leading to subsequent neurological deficits. In light of this, safeguarding astrocytes from injury emerges as a promising strategy for NMOSD therapeutics [42]. However, the specific regulatory mechanism underlying the toxic damage to astrocytes in this process remains unclear. Studies have suggested the pivotal role of TDP43 in the pathogenesis of various CNS disorders, where its mislocalization, depletion, or mutation correlates strongly with notable neurological impairments [16]. TDP43 has also been linked to microglial activation in neurodegenerative diseases [43]. Particularly, in patients with ALS, astrocytes derived from pluripotent stem cells exhibit abnormal aggregation of TDP43 in the cytoplasm [18]. These studies suggest the crucial role of TDP43 in neurological dysfunction in CNS disorders. Despite

these advancements, the involvement of TDP43 in astrocyte activation within the context of NMOSD remains unclear. Research has shown that abnormal aggregation of TDP43 on mitochondria leads to mitochondrial dysfunction [22, 23, 38]. Research based on patient samples indicates NMOSD as a mitochondrial disease [7], prompting our investigation into the potential role of TDP43 in NMOSD-induced astrocyte activation and mitochondrial dysfunction. In this study, we observed heightened levels of TDP43 in both CSF and serum samples from NMOSD patients. Notably, we observed that the knockdown of astrocytic TDP43 ameliorated the injuries induced by AQP4-IgG in both *in vitro* and *in vivo* NMOSD models, whereas the overexpression of TDP43 amplified the extent of NMOSD-induced damages. This discovery sheds light on the impact of TDP43 abnormalities on facilitating inflammatory activation of astrocytes during NMOSD, significantly spotlighting TDP43 as a potential therapeutic target in NMOSD treatment. The role of AQP4-IgG and complement in inducing astrocytic death via C5b-9 activation and MAC formation in NMOSD has been well established. However, the mechanism by which they lead to TDP-43 proteinopathy remains unclear. A recent study suggests that the activation of the complement system induces the development of TDP-43 proteinopathy [44], which is consistent with our results. It is possible that complement activation might create a cascade of events that contribute to the accumulation and mislocalization of TDP-43. However, it should be noted that further research is needed to fully understand the pathomechanism.

Like NMOSD, multiple sclerosis is another major demyelinating disorder in the central nervous system. As mentioned by previous studies, altered expression and mislocalization of TDP-43 proteinopathy has been reported in multiple sclerosis and its animal models [45–48]. TDP-43 proteinopathy in multiple sclerosis may play a significant role in the pathogenesis of the disease. The presence of abnormal TDP-43 protein aggregation and dysfunction could contribute to neuronal damage and degeneration [45–48]. In our study, we discover the role of abnormal astrocytic TDP43 expression contribute to demyelination in NMOSD, which is consistent with the discovery in multiple sclerosis. Taken together, our results showed that TDP-43 might be a promising therapeutic strategy for the treatment of demyelinating disorder.

Our investigation propounds that TDP43 may be intricately involved in the pathological process of astrocyte A1 type activation within the context of NMOSD, presumably through mechanisms tied to TDP43-induced mitochondrial impairment. Our findings delineate that NMOSD prompts the translocation of TDP43 to mitochondria, which leads to mitochondrial dysfunction and

the release of mtDNA into the cytoplasm. This mtDNA acts as a key activator of the cGAS/STING pathway [28], proposing a mechanism whereby TDP43 may influence A1 type activation of astrocytes through the mtDNA/cGAS/STING axis, thereby propelling neuronal damage. The cGAS/STING signaling pathway is recognized for its pivotal role in a myriad of pathological states, encompassing infections [49], tumors [50], and immune-mediated responses [51], and is notably implicated in age-related inflammation as well as neurodegenerative conditions [52]. Recent studies have unveiled the role of cGAS/STING in astrocyte senescence in the context of Parkinson's disease [53, 54]. However, the role of cGAS/STING in astrocytic activation and pathology of NMOSD has remained an elusive terrain. To the best of our knowledge, this research pioneers in unveiling the contributory role of cGAS/STING axis in astrocytic activation, notably within the scope of NMOSD. Additionally, our observations spotlight the activation of the cGAS/STING axis in NMOSD, underlining a potential contribution towards astrocyte activation. Our study offers new avenues for attenuating the detrimental effects of astrocyte activation and the ensuing neurodegenerative outcomes in NMOSD.

Conclusions

In conclusion, our data suggest that TDP43 exacerbates the inflammatory activation of astrocytes through upregulation of the mtDNA/cGAS/STING signaling pathway, by underscoring the pathological role of TDP43 and linking it with key inflammatory mechanisms within NMOSD. These insights thus open up new avenues for research and therapeutic development, aiming at ameliorating the debilitating impacts of NMOSD through targeted intervention in the TDP43/mitochondrial dysfunction axis.

Abbreviations

ALS	Amyotrophic lateral sclerosis
AQP4	Aquaporin 4
cGAMP	2'3' cyclic GMP-AMP
cGAS	Cyclic GMP-AMP synthase
ELISA	Enzyme-linked immunosorbent assay
ER	Endoplasmic reticulum
MBP	Myelin basic protein
MMP	Mitochondrial membrane potential
mtDNA	Mitochondrial DNA
NMOSD	Neuromyelitis optica spectrum disorder
STING	Stimulator of interferon genes
TDP43	Transactivating response region DNA binding protein 43
TFAM	Mitochondrial transcription factor A

Supplementary Information

The online version contains supplementary material available at <https://doi.org/10.1186/s12974-025-03348-z>.

Supplementary Material 1

Acknowledgements

We thank Professor Qiang Liu of Tianjin Medical University for revising the manuscript.

Author contributions

Zhuhe Liu, Bingtian Xu, Haixia Wen, Kechun Chen, Jingfan Lin, and Yuanyuan Wang completed the experiments and analyzed the data. Yunmeng Bai and Jigang Wang analyzed the result of single-nucleus RNA sequencing. Zhuhe Liu wrote the first draft of the manuscript. Honghao Wang, Fudong Shi, and Bingtian Xu designed experiments and revised the manuscript. Honghao Wang, Fudong Shi, and Jigang Wang supervised the research. Haitao Wang and Jiangping Xu provided the equipment for the experiments.

Funding

This work was supported by grants from the National Natural Science Foundation of China (No. 82371364, 82401575), the Guangdong Provincial Science and Technology plan projects (No. 2023A1515011372), and the Science and Technology Projects of Guangzhou (No. 2023A03J0960, 2024A03J0965, and 2024A04J4016).

Data availability

The data which support this study are available from the corresponding authors on reasonable request.

Declarations

Ethics approval and consent to participate

Full informed consent was obtained from patients and the collection of CSF and serum was conducted under the approval of the Research ethics committee and performed in accordance with the ethical standards laid down in an appropriate version of the 1964 Declaration of Helsinki. Animal research reports comply with the NIH Guide for the Care and Use of Laboratory Animals (NIH, revised 1996) and ARRIVE guidelines 3.0. All animal experiments were approved by the Experimental Animal Ethics Committee of Southern Medical University.

Consent for publication

All authors approved the final manuscript and the submission.

Competing interests

The authors declare no competing interests.

Received: 14 October 2024 / Accepted: 15 January 2025

Published online: 22 January 2025

References

- Jarius S, Paul F, Weinschenker BG, Levy M, Kim HJ, Wildemann B. Neuromyelitis Optica. *Nat Rev Dis Primers*. 2020;6:85.
- Zhu W, Zhang Y, Wang Z, Fu Y, Yan Y. Monoclonal antibody-based treatments for Neuromyelitis Optica Spectrum Disorders: from bench to Bedside. *Neurosci Bull*. 2020;36:1213–24.
- Lucchinetti CF, Guo Y, Popescu BF, Fujihara K, Itoyama Y, Misu T. The pathology of an autoimmune astrocytopathy: lessons learned from neuromyelitis optica. *Brain Pathol*. 2014;24:83–97.
- Ratelade J, Asavapanumas N, Ritchie AM, Wemlinger S, Bennett JL, Verkman AS. Involvement of antibody-dependent cell-mediated cytotoxicity in inflammatory demyelination in a mouse model of neuromyelitis optica. *Acta Neuropathol*. 2013;126:699–709.
- Morch MT, Khorooshi R, Marczyńska J, Dubik M, Nielsen S, Nieland JD, Asgari N, Owens T. Mitochondria-A target for attenuation of astrocyte pathology. *J Neuroimmunol*. 2021;358:577657.
- Nohara S, Ishii A, Yamamoto F, Yanagiha K, Moriyama T, Tozaka N, Miyake Z, Yatsuga S, Koga Y, Hosaka T, et al. GDF-15, a mitochondrial disease biomarker, is associated with the severity of multiple sclerosis. *J Neurol Sci*. 2019;405:116429.
- Foolad F, Khodaghali F, Nabavi SM, Javan M. Changes in mitochondrial function in patients with neuromyelitis optica; correlations with motor and cognitive disabilities. *PLoS ONE*. 2020;15:e0230691.

8. Hokari M, Yokoseki A, Arakawa M, Saji E, Yanagawa K, Yanagimura F, Toyoshima Y, Okamoto K, Ueki S, Hatase T, et al. Clinicopathological features in anterior visual pathway in neuromyelitis optica. *Ann Neurol*. 2016;79:605–24.
9. Zveik O, Rechtman A, Haham N, Adini I, Canello T, Lavon I, Brill L, Vaknin-Dembinsky A. Sera of Neuromyelitis Optica patients increase BID-Mediated apoptosis in astrocytes. *Int J Mol Sci*. 2022;23:7117.
10. Shimizu M, Okuno T, Kinoshita M, Sumi H, Fujimura H, Yamashita K, Sugimoto T, Sakakibara S, Sakakibara K, Koda T, et al. Mitochondrial DNA enhance innate immune responses in neuromyelitis optica by monocyte recruitment and activation. *Sci Rep*. 2020;10:13274.
11. Gollihue JL, Norris CM. Astrocyte mitochondria: Central players and potential therapeutic targets for neurodegenerative diseases and injury. *Ageing Res Rev*. 2020;59:101039.
12. Lee DS, Kim TH, Park H, Kim JE. CDDO-Me attenuates clasmatodendrosis in CA1 astrocyte by inhibiting HSP25-AKT mediated DRP1-S637 phosphorylation in Chronic Epilepsy rats. *Int J Mol Sci*. 2022;23.
13. Kaur MM, Sharma DS. Mitochondrial repair as potential pharmacological target in cerebral ischemia. *Mitochondrion*. 2022;63:23–31.
14. Mi Y, Qi G, Vitali F, Shang Y, Raikes AC, Wang T, Jin Y, Brinton RD, Gu H, Yin F. Loss of fatty acid degradation by astrocytic mitochondria triggers neuroinflammation and neurodegeneration. *Nat Metab*. 2023;5:445–65.
15. Wang Y, Xia Y, Kou L, Yin S, Chi X, Li J, Sun Y, Wu J, Zhou Q, Zou W, et al. Astrocyte-to-neuron reprogramming and crosstalk in the treatment of Parkinson's disease. *Neurobiol Dis*. 2023;184:106224.
16. Tziortzouda P, Van Den Bosch L, Hirth F. Triad of TDP43 control in neurodegeneration: autoregulation, localization and aggregation. *Nat Rev Neurosci*. 2021;22:197–208.
17. Klim JR, Williams LA, Limone F, Guerra San Juan I, Davis-Dusenbery BN, Mordes DA, Burberry A, Steinbaugh MJ, Gamage KK, Kirchner R, et al. ALS-implicated protein TDP-43 sustains levels of STMN2, a mediator of motor neuron growth and repair. *Nat Neurosci*. 2019;22:167–79.
18. Serio A, Bilcan B, Barmada SJ, Ando DM, Zhao C, Siller R, Burr K, Haghi G, Story D, Nishimura AL, et al. Astrocyte pathology and the absence of non-cell autonomy in an induced pluripotent stem cell model of TDP-43 proteinopathy. *Proc Natl Acad Sci U S A*. 2013;110:4697–702.
19. Licht-Murava A, Meadows SM, Palaguachi F, Song SC, Jackvony S, Bram Y, Zhou C, Schwartz RE, Froemke RC, Orr AL, Orr AG. Astrocytic TDP-43 dysregulation impairs memory by modulating antiviral pathways and interferon-inducible chemokines. *Sci Adv*. 2023;9:eade1282.
20. Tong J, Huang C, Bi F, Wu Q, Huang B, Liu X, Li F, Zhou H, Xia XG. Expression of ALS-linked TDP-43 mutant in astrocytes causes non-cell-autonomous motor neuron death in rats. *Embo j*. 2013;32:1917–26.
21. Peng AYT, Agrawal I, Ho WY, Yen YC, Pinter AJ, Liu J, Phua QXC, Koh KB, Chang JC, Sanford E, et al. Loss of TDP-43 in astrocytes leads to motor deficits by triggering A1-like reactive phenotype and triglial dysfunction. *Proc Natl Acad Sci U S A*. 2020;117:29101–12.
22. Huang C, Yan S, Zhang Z. Maintaining the balance of TDP-43, mitochondria, and autophagy: a promising therapeutic strategy for neurodegenerative diseases. *Transl Neurodegener*. 2020;9:40.
23. Zuo X, Zhou J, Li Y, Wu K, Chen Z, Luo Z, Zhang X, Liang Y, Esteban MA, Zhou Y, Fu XD. TDP-43 aggregation induced by oxidative stress causes global mitochondrial imbalance in ALS. *Nat Struct Mol Biol*. 2021;28:132–42.
24. Civril F, Deimling T, de Oliveira Mann CC, Ablasser A, Moldt M, Witte G, Hornung V, Hopfner KP. Structural mechanism of cytosolic DNA sensing by cGAS. *Nature*. 2013;498:332–7.
25. Sun L, Wu J, Du F, Chen X, Chen ZJ. Cyclic GMP-AMP synthase is a cytosolic DNA sensor that activates the type I interferon pathway. *Science*. 2013;339:786–91.
26. Hu X, Zhang H, Zhang Q, Yao X, Ni W, Zhou K. Emerging role of STING signaling in CNS injury: inflammation, autophagy, necroptosis, ferroptosis and pyroptosis. *J Neuroinflammation*. 2022;19:242.
27. Ferencsik AS, Smallwood MJ, Moore A, Liddle C, Newcombe J, Holley J, Whatmore J, Gutowski NJ, Eggleton P. STING-Triggered CNS Inflammation in Human Neurodegenerative Diseases. *Biomedicines*. 2023;11.
28. Riley JS, Tait SW. Mitochondrial DNA in inflammation and immunity. *EMBO Rep*. 2020;21:e49799.
29. Ma C, Liu Y, Li S, Ma C, Huang J, Wen S, Yang S, Wang B. Microglial cGAS drives neuroinflammation in the MPTP mouse models of Parkinson's disease. *CNS Neurosci Ther*. 2023;29:2018–35.
30. Griggs RC, Mao ZF, Qiu W, Hu XQ, Wingerchuk DM, Weinshenker BG. International consensus diagnostic criteria for neuromyelitis optica spectrum disorders. *Neurology*. 2016;86:491–.
31. Serizawa K, Miyake S, Katsura Y, Yorozu K, Kurasawa M, Tomizawa-Shinohara H, Yasuno H, Matsumoto Y. Intradermal AQP4 peptide immunization induces clinical features of neuromyelitis optica spectrum disorder in mice. *J Neuroimmunol*. 2023;380:578109.
32. Bai Y, Liu Z, Qian T, Peng Y, Ma H, Hu H, Cheng G, Wen H, Xie L, Zheng D, et al. Single-nucleus RNA sequencing unveils critical regulators in various hippocampal neurons for anti-N-methyl-D-aspartate receptor encephalitis. *Brain Pathol*. 2023;33:e13156.
33. Li WP, Su XH, Hu NY, Hu J, Li XW, Yang JM, Gao TM. Astrocytes mediate cholinergic regulation of adult hippocampal neurogenesis and memory through M(1) muscarinic receptor. *Biol Psychiatry*. 2022;92:984–98.
34. Wei D, Niu B, Zhai B, Liu XB, Yao YL, Liang CC, Wang P. Expression profiles and function prediction of tRNA-derived fragments in glioma. *BMC Cancer*. 2023;23:1015.
35. Li J, Lu Y, Lin G. Blocking cGAS/STING signaling protects against sepsis-associated acute liver injury. *Int Immunopharmacol*. 2022;113:109276.
36. Liu Z, Wang Y, Ding Y, Wang H, Zhang J, Wang H. CXCL7 aggravates the pathological manifestations of neuromyelitis optica spectrum disorder by enhancing the inflammatory infiltration of neutrophils, macrophages and microglia. *Clin Immunol*. 2022;245:109139.
37. Zhao M, Wang Y, Li L, Liu S, Wang C, Yuan Y, Yang G, Chen Y, Cheng J, Lu Y, Liu J. Mitochondrial ROS promote mitochondrial dysfunction and inflammation in ischemic acute kidney injury by disrupting TFAM-mediated mtDNA maintenance. *Theranostics*. 2021;11:1845–63.
38. Yu CH, Davidson S, Harapas CR, Hilton JB, Mlodzianoski MJ, Laohamonthonkul P, Louis C, Low RRR, Moecking J, De Nardo D, et al. TDP-43 triggers mitochondrial DNA release via mPTP to activate cGAS/STING in ALS. *Cell*. 2020;183:636–e649618.
39. Chen C, Xu P. Cellular functions of cGAS-STING signaling. *Trends Cell Biol*. 2023;33:630–48.
40. Liu Y, Huang Z, Zhang TX, Han B, Yang G, Jia D, Yang L, Liu Q, Lau AYL, Paul F, et al. Bruton's tyrosine kinase-bearing B cells and microglia in neuromyelitis optica spectrum disorder. *J Neuroinflammation*. 2023;20:309.
41. Matsumoto Y, Kaneko K, Takahashi T, Takai Y, Namatame C, Kuroda H, Misu T, Fujihara K, Aoki M. Diagnostic implications of MOG-IgG detection in sera and cerebrospinal fluids. *Brain*. 2023;146:3938–48.
42. Tradtrantip L, Zhang H, Anderson MO, Saadoun S, Phuan PW, Papadopoulos MC, Bennett JL, Verkman AS. Small-molecule inhibitors of NMO-IgG binding to aquaporin-4 reduce astrocyte cytotoxicity in neuromyelitis optica. *FASEB j*. 2012;26:2197–208.
43. Xie M, Liu YU, Zhao S, Zhang L, Bosco DB, Pang YP, Zhong J, Sheth U, Martens YA, Zhao N, et al. TREM2 interacts with TDP-43 and mediates microglial neuroprotection against TDP-43-related neurodegeneration. *Nat Neurosci*. 2022;25:26–38.
44. Zhang J, Velmeshev D, Hashimoto K, Huang Y-H, Hofmann JW, Shi X, Chen J, Leidal AM, Dishart JG, Cahill MK, et al. Neurotoxic microglia promote TDP-43 proteinopathy in progranulin deficiency. *Nature*. 2020;588:459–65.
45. Masaki K, Sonobe Y, Ghadge G, Pytel P, Lépine P, Pernin F, Cui Q-L, Antel JP, Zandee S, Prat A, Roos RP. RNA-binding protein altered expression and mislocalization in MS. *Neurol Neuroimmunol Neuroinflammation*. 2020;7.
46. Salapa HE, Hutchinson C, Popescu BF, Levin MC. Neuronal RNA-binding protein dysfunction in multiple sclerosis cortex. *Ann Clin Transl Neurol*. 2020;7:1214–24.
47. Salapa HE, Libner CD, Levin MC. Dysfunctional RNA-binding protein biology and neurodegeneration in experimental autoimmune encephalomyelitis in female mice. *J Neurosci Res*. 2019;98:704–17.
48. Semler BL, Masaki K, Sonobe Y, Ghadge G, Pytel P, Roos RP. TDP-43 proteinopathy in Theiler's murine encephalomyelitis virus infection. *PLoS Pathog*. 2019;15:e1007574.
49. Sanz MA, Polo M, Rodríguez-Pulido M, Bommanna RH, Saiz M. The antiviral response triggered by the cGAS/STING pathway is subverted by the foot-and-mouth disease virus proteases. *Cell Mol Life Sci*. 2024;81:15.
50. Samson N, Ablasser A. The cGAS-STING pathway and cancer. *Nat Cancer*. 2022;12.
51. Tong J, Song J, Zhang W, Zhai J, Guan Q, Wang H, Liu G, Zheng C. When DNA-damage responses meet innate and adaptive immunity. *Cell Mol Life Sci*. 2024;81:185.
52. Xie XC, Ma GQ, Li XH, Zhao JB, Zhao Z, Zeng JX. Activation of innate immune cGAS-STING pathway contributes to Alzheimer's pathogenesis in 5xFAD mice. *Nat Aging*. 2023;3:202–.
53. Wang M, Tian T, Zhou H, Jiang SY, Jiao YY, Zhu Z, Xia J, Ma JH, Du RH. Metformin normalizes mitochondrial function to delay astrocyte senescence in a

mouse model of Parkinson's disease through Mfn2-cGAS signaling. *J Neuroinflamm.* 2024;21:17.

54. Jiang SY, Tian T, Yao H, Xia XM, Wang C, Cao L, Hu G, Du RH, Lu M. The cGAS-STING-YY1 axis accelerates progression of neurodegeneration in a mouse model of Parkinson's disease via LCN2-dependent astrocyte senescence. *Cell Death Differ.* 2023;30:2280–92.

Publisher's note

Springer Nature remains neutral with regard to jurisdictional claims in published maps and institutional affiliations.